Geosci. Model Dev., 9, 2665–2684, 2016
www.geosci-model-dev.net/9/2665/2016/
doi:10.5194/gmd-9-2665-2016

Geoscientific Model Development
Open Access

A 1/16° eddying simulation of the global NEMO sea-ice–ocean system

Doroteaciro Iovino[1], **Simona Masina**[1,2], **Andrea Storto**[1], **Andrea Cipollone**[1], **and Vladimir N. Stepanov**[1]

[1]Fondazione Centro Euro-Mediterraneo sui Cambiamenti Climatici (CMCC), Bologna, Italy
[2]Istituto Nazionale di Geofisica e Vulcanologia (INGV), Bologna, Italy

Correspondence to: Doroteaciro Iovino (dorotea.iovino@cmcc.it)

Received: 7 December 2015 – Published in Geosci. Model Dev. Discuss.: 18 January 2016
Revised: 16 June 2016 – Accepted: 11 July 2016 – Published: 12 August 2016

Abstract. Analysis of a global eddy-resolving simulation using the NEMO general circulation model is presented. The model has 1/16° horizontal spacing at the Equator, employs two displaced poles in the Northern Hemisphere, and uses 98 vertical levels. The simulation was spun up from rest and integrated for 11 model years, using ERA-Interim reanalysis as surface forcing. Primary intent of this hindcast is to test how the model represents upper ocean characteristics and sea ice properties.

Analysis of the zonal averaged temperature and salinity, and the mixed layer depth indicate that the model average state is in good agreement with observed fields and that the model successfully represents the variability in the upper ocean and at intermediate depths. Comparisons against observational estimates of mass transports through key straits indicate that most aspects of the model circulation are realistic. As expected, the simulation exhibits turbulent behaviour and the spatial distribution of the sea surface height (SSH) variability from the model is close to the observed pattern. The distribution and volume of the sea ice are, to a large extent, comparable to observed values.

Compared with a corresponding eddy-permitting configuration, the performance of the model is significantly improved: reduced temperature and salinity biases, in particular at intermediate depths, improved mass and heat transports, better representation of fluxes through narrow and shallow straits, and increased global-mean eddy kinetic energy (by ∼ 40 %). However, relatively minor weaknesses still exist such as a lower than observed magnitude of the SSH variability. We conclude that the model output is suitable for broader analysis to better understand upper ocean dynamics and ocean variability at global scales. This simulation represents a major step forward in the global ocean modelling at the Euro-Mediterranean Centre on Climate Change and constitutes the groundwork for future applications to short-range ocean forecasting.

1 Introduction

The global ocean is a highly turbulent system over a wide range of space and timescales. Both satellite and in situ data show that mesoscale eddies pervade the ocean at all latitude bands. Eddies usually account for the peak in the kinetic energy (KE) spectrum and most of their energy is generated and maintained by baroclinic instabilities of large-scale flows. Those processes play a substantial role in the dynamics of the global ocean, e.g. transporting and mixing temperature and salinity, exchanging energy and momentum with the mean flow, controlling the mechanisms of deep water spreading and deep convection preconditioning, and modulating air-sea interactions (see e.g. Morrow and Le Traon, 2012). The dominant length scale of these eddies varies greatly with latitude, stratification, and ocean depth. Mesoscale eddies typically have horizontal scales of the order of the first baroclinic Rossby radius of deformation, varying roughly from 200 km in the tropics to 10–20 km at 50–60° (Chelton et al., 1998), vertical scales ranging from the pycnocline depth to the full ocean depth, and timescales of weeks and months.

Global numerical ocean models, with spatial resolutions ranging from hundred down to a few kilometres, often include both regions where the dominant eddy scales are well resolved and regions where the model resolution is too coarse for eddies to form and hence eddy effects have to be parameterized. In the context of ocean modelling, a model will be eddy rich as long as it uses a horizontal grid mesh whose resolution is fine enough to explicitly (albeit partially) resolve baroclinic and barotropic instability processes, i.e. the grid spacing is finer than the first baroclinic Rossby radius of deformation. Hallberg (2013) showed the model horizontal resolution required to resolve the first baroclinic deformation radius with two grid points, based on a Mercator grid. From his analysis, 1/4° Mercator spacing is insufficient to resolve mesoscale eddies that have a typical scale of 50 km at midlatitudes. Since the milestone paper by Smith et al. (2000), eddy effects are considered explicitly modelled when the horizontal grids are refined to at least 1/10° (ca. 12 km); however, such resolution adequately describes both mesoscale variability and western boundary currents only for latitudes lower than $\sim 50°$. Resolving mesoscale eddy variability remains elusive at higher latitudes. For example, in the Arctic Ocean where the first Rossby radius decreases down to few kilometres on the continental shelf and in weakly stratified regions, resolution up to about 1/10° only permits eddies at best (Nurser and Bacon, 2014).

Operational oceanography for a variety of different applications such as search and rescue, fisheries, and oil spills requires global ocean forecasting systems to reach kilometric scales in coastal areas. This demand is also fostered by the continuous increase of resolution in numerical weather prediction models and the design of next-generation satellite altimetry missions (Le Traon et al., 2015) that will aim to better capture the ocean mesoscale variability.

These considerations motivate the push toward fully mesoscale eddying ocean models, where the full dynamics and life cycle of baroclinic eddies can be realistically represented over almost the entire global domain. Thanks to progress in ocean modelling and the advances in high performance computing resources over the last decade, numerical simulations at higher resolution are now a realistic choice to bring new insights into the oceanic physical processes and to find application in ocean modelling and forecasting. During the last decade, an extensive effort has been made to simulate eddying ocean, and different models have been implemented in regional, near-global, and fully global domains (e.g. Maltrud and McClean, 2005; Chassignet et al., 2009; Oke et al., 2013; Drakkar Group, 2014; Metzger et al., 2014; Dupont et al., 2015). In this context, we developed a global eddying configuration, where eddying means that the numerical simulation is eddy-resolving in the majority of deep ocean regions, while it is mostly eddy-permitting on the continental shelves or in weakly stratified polar latitudes. Although the increase of resolution does not necessarily lead per se to an improved representation of the ocean general circulation, the aim of this work is to evaluate the effect of the explicit solution of eddy dynamics at low and midlatitudes on the large-scale dynamics of a high-resolution global ocean model, compared to a coarser resolution configuration. Thus, this paper seeks to present the general characteristics of an 11-year spin-up simulation performed with the ocean model configuration, hereafter called GLOB16, at 1/16° (ca. 6.9 km) equatorial resolution, which is performed using the state-of-the-art modelling framework NEMO (Nucleus for European Modelling of the Ocean). The numerical model is a coupled ocean/sea-ice model, including a three-dimensional, primitive equation ocean general circulation model and a dynamic–thermodynamic sea ice model. So far, GLOB16 represents the NEMO global configuration having the highest horizontal resolution and is a foothold that opens the way for the development of a new, operational short-term ocean forecast system meant to serve as the backbone for downscaling coastal and regional applications to develop services for the global coastal ocean.

The paper is organized as follows. Section 2 describes the model set-up, while model analysis is found in Sect. 3. We rely on comparisons with observations, as well as with a twin eddy-permitting experiment, called GLOB4, as a means of assessing the quality of GLOB16 solution. Conclusions follow in Sect. 4.

2 Model configuration

GLOB16 is a global, eddying configuration of the ocean and sea ice system based on version 3.4 of the NEMO ocean model (Madec and the NEMO team, 2012). The ocean component OPA is a finite difference, hydrostatic, primitive equation ocean general circulation model, with a free sea surface. The ocean component is coupled to the Louvain-la-Neuve sea Ice Model (LIM2) (Fichefet and Morales Maqueda, 1997). The ice dynamics are calculated according to external forcing from wind stress, ocean stress, and sea surface tilt and internal ice stresses using C grid formulation (Bouillon et al., 2009). The elastic–viscous–plastic formulation by Hunke and Dukowicz (1997) is used. The key features of the configuration follow in this section, while a comprehensive technical description of GLOB16 is given in Iovino et al. (2014).

2.1 Mesh

GLOB16 makes use of a nonuniform tripolar grid, computed at CMCC following the semi-analytical method of Madec and Imbard (1996). The horizontal grid has a 1/16° resolution at the Equator, corresponding to 6.9 km, that increases poleward as cosine of latitude, leading to 5762×3963 grid points horizontally. The grid consists of an isotropic Mercator grid from 60° S to 20° N. The meridional scale factor is maintained constant at 3 km south of 60° S. The location of the geographical South Pole is conserved and the domain extents southwards to 78° S, including the ice shelf edge in the Weddell and Ross seas. North of 20° N, the grid consists of a non-geographic quasi-isotropic grid. To avoid singularities associated with the convergence of meridians at the North Pole, two distinct poles are introduced, the locations of which are such that the minimum horizontal resolution is ~ 2 km around Victoria Island. Ocean and sea ice are on the same horizontal grid. The vertical coordinate system is based on fixed depth levels and consists of 98 vertical levels with a grid spacing increasing from approximately 1 m near the surface to 160 m in the deep ocean.

2.2 Bathymetry

The GLOB16 bathymetry is generated from three distinct topographic products: ETOPO2 (US Department of Commerce, 2006) is used for the deep ocean, GEBCO (IOC, IHO and BODC, 2003) for the continental shelves shallower than 300 m, and Bedmap2 (Fretwell et al., 2013) for the Antarctic region, south of 60° S. The result is modified by two passes of a uniform Shapiro filter, and finally hand editing is performed in key areas. The Black Sea is connected to the Marmara Sea through a 1-grid-point-wide channel. The Caspian Sea is derived from ETOPO2. The maximum depth allowed in the model is 6000 m, and the minimum depth is set to 10 m. Bottom topography is represented as partial steps (Barnier et al., 2006).

2.3 Parameterizations

In our simulation, a linearized free-surface formulation is used (Roullet and Madec, 2000) and a free-slip lateral friction condition is applied at the lateral boundaries. Biharmonic viscosity and diffusivity schemes are used in the horizontal directions in the equations of momentums and tracers, respectively. The values decrease poleward as the cube of the grid cell size. Tracer advection uses a total variance dissipation (TVD) scheme (Zalesak, 1979). Vertical mixing is achieved using the turbulent kinetic energy (TKE) closure scheme (Blanke and Delecluse, 1993). Unresolved vertical mixing processes are represented by a background vertical eddy diffusivity of $1.2 \times 10^{-5}\,\mathrm{m^2\,s^{-1}}$ and a globally constant background viscosity of $1.2 \times 10^{-4}\,\mathrm{m^2\,s^{-1}}$. Background coefficients of vertical diffusion and viscosity represent the vertical mixing induced by unresolved processes in the model. Vertical eddy mixing of both momentum and tracers is enhanced in case of static instability. The turbulent closure model does not apply any specific modification in ice-covered regions. Bottom friction is quadratic. A diffusion bottom boundary layer parameterization is used for tracers.

2.4 Initialization

The simulation is started from a state of rest in January 2003, with initial conditions for temperature and salinity derived from the 1995–2004 decade of the World Ocean Atlas 2013 set of climatologies (WOA13; Locarnini et al., 2013; Zweng et al., 2013). The initial conditions for the sea ice (ice concentration, ice thickness) correspond to mean January 2003 produced by a global ocean reanalysis run at 1/4° horizontal resolution (Storto et al., 2016).

2.5 Forcing

Forcing fields are provided from ERA-Interim global atmospheric reanalysis (Dee et al., 2011), released by European Centre for Medium-Range Weather Forecasts (ECMWF), with 0.75° spatial resolution. The turbulent variables are 3 hourly and radiative and freshwater fluxes are daily. The surface boundary conditions are prescribed to the model using the bulk formulae proposed by Large and Yeager (2004). The forcing routine and the ice model are called every four time steps (ca. every 13 min). A monthly climatology of coastal runoff is derived from Dai and Trenberth (2002) and Dai et al. (2009), with a global annual discharge of ~ 1.32 Sv ($1\,\mathrm{Sv} = 10^6\,\mathrm{m^3\,s^{-1}}$), and is applied along the land mask. The fresh water is added to the surface, assumed to be fresh and at local sea surface temperature (SST). As the thickness of the uppermost level is 0.4 m, diurnal cycle is imposed on solar flux: the daily averaged short wave flux is spread over the day according to time and geographical position (Bernie et al., 2007). The mean sea level is free to drift. Shortwave penetration is applied through the RGB (red–green–blue) formulation that splits the visible light into three wavebands. The penetration is modulated by a constant chlorophyll value.

2.6 Restoring and spin-up

To avoid drifts in salinity and eventual impacts on the overturning circulation, the sea surface salinity (SSS) is restored toward the monthly objective analyses from the EN4 data set of the Met Office Hadley Centre (Good et al., 2013), with a timescale of 300 days for the upper 50 m. The SST is restored towards the NOAA Optimum Interpolation 1/4° Daily Sea Surface Temperature Analysis (Reynolds et al., 2007) with a constant damping term of $200\,\mathrm{W\,m^{-2}\,K^{-1}}$, which corresponds to a restoring time of 12 days. The restoring is identical for the open sea and ice-covered areas. The SST relaxation is implemented to limit the propagation of the atmospheric forcing biases into the upper ocean and thus, with this constrain, reproduce a fairly realistic variability of the upper ocean heat content.

The time step was set to 20 s for the first 3 days of the simulation and then increased progressively to reach 200 s at the 60th day. The model ran for 11 years through the end of 2013, which appears to be a sufficient amount of time for the near-surface velocity field to adjust to the initial density field and for mesoscale processes in the upper ocean to have reached a quasi-equilibrium, while the deep ocean takes much longer to reach steady state. This simulation may therefore be appropriate for studying the dynamics of the ocean circulation on short timescales but not for studying the long-term evolution of deep-water masses or climate variability. The GLOB16 experiment was performed using 4080 CPU cores on an IBM System x iDataPlex supercomputer. Per simulated year, it required 112 000 CPU hours and generated ~ 3 Tb of output files.

2.7 Output and analysis strategy

Model outputs are archived as successive 5-day means throughout the whole integration and post-processed to monthly and annual means. The first simulated year, 2003, is disregarded because of the initial model adjustment; variability in time is analysed over the period 2004–2013, while mean values are computed over the last 5 years of integrations, from 2009 to 2013, unless otherwise indicated.

2.8 Eddy-permitting configuration

For comparison purposes, we performed a twin experiment, GLOB4, at eddy-permitting resolution, which is also based on version 3.4 of NEMO. This configuration is a global implementation on an ORCA-like tri-polar grid (Barnier et al., 2006), with a horizontal grid spacing of 0.25° at global scale (1442 × 1021 grid points). The effective resolution is $\sim$27.75 km at the Equator and increases as the cosine of latitude with minima of 3.1 km (5.6 km) in the meridional (zonal) direction. The model has 75 vertical levels where the level spacing increases from 1 m near the surface to 200 m at 6000 m. The bathymetry used in GLOB4 is based on the combination of GEBCO in coastal regions and ETOPO2 in open-ocean areas. A uniform Shapiro filter is applied twice, and hand editing is performed in a few key areas. Bottom topography is represented as partial steps.

GLOB4 has the sea ice component, atmospheric forcing, bulk formulation, and tracer restoring in common with GLOB16. It employs the same numerical schemes and parameterizations as GLOB16, except for the resolution-dependent parameters. In particular, the key modifications from GLOB4 to GLOB16 in setting the ocean parameters are a reduction in the biharmonic viscosity from -1.8×10^{11} to $-0.5 \times 10^{9}\,\mathrm{m^4\,s^{-1}}$, a reduction in the lateral tracer diffusion from 300 to 80 $\mathrm{m^2\,s^{-1}}$; a reduction in the time step from 1080 to 200 s. We attribute the main differences between the two model configurations to the increase of ocean resolution, in the horizontal and vertical grid.

3 Model validation

The main objective of this section is to present an overview of the characteristics of the GLOB16 simulation, evaluate its quality against recent observations, and highlight the effect of eddying resolution against the eddy-permitting run.

The spin-up of the circulation, as measured by the total KE (defined as $0.5\,(u^2+v^2)$, where u and v are the 5-day averages of the horizontal velocity components), potential temperature, and salinity averaged over the whole domain, is shown in Fig. 1,and demonstrates the extent to which a quasi-steady state has been reached at the end of the simulation. The total KE of the system increases rapidly during the first simulated year (2003, not shown) and approaches $\sim 12\,\mathrm{cm^2\,s^{-2}}$ at the beginning of 2004, indicating a baro-

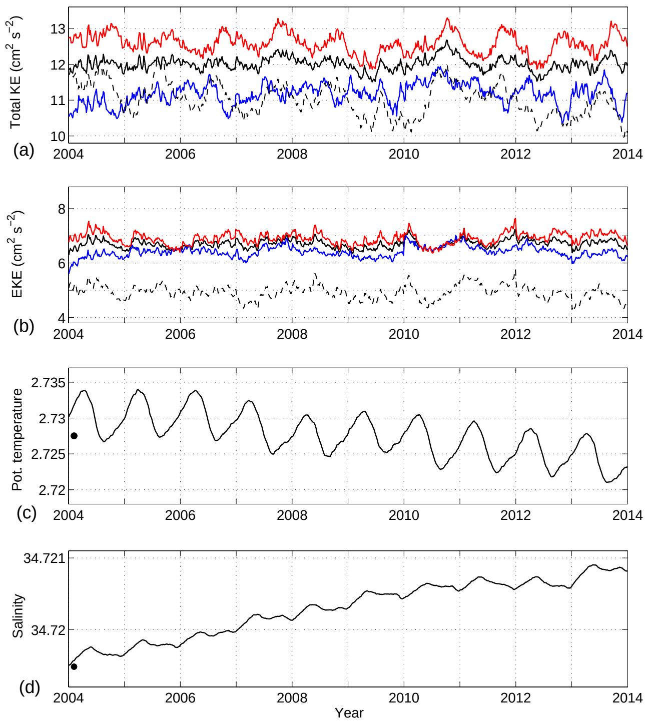

Figure 1. Time variations of volume-averaged **(a)** total kinetic energy (KE; in $\mathrm{cm^2\,s^{-2}}$), where the black line represents the global basin-mean value and the red (blue) the contribution of the Southern (Northern) Hemisphere in GLOB16. Thin-dashed line represents the basin-mean total KE in GLOB4. **(b)** As panel **(a)** but for eddy kinetic energy (EKE; in $\mathrm{cm^2\,s^{-2}}$). The seasonal cycle of the mean field has been removed. **(c)** Potential temperature in °C; **(d)** salinity in psu. Black circles indicate temperature and salinity initial values.

clinic adjustment of the velocity field to the initial density field. Then, the kinetic energy fluctuates between 11.5 and 12.5 $\mathrm{cm^2\,s^{-2}}$ for the rest of the simulation, with the highest contribution given by the Southern Ocean (Fig. 1a). Most of the kinetic energy is in the eddy field: the mean GLOB16 eddy kinetic energy (EKE, computed from the 5-day velocity fields using the equation $0.5\,(u'^2+v'^2)$, where primes denote deviations from the annual-mean velocities, $(u',v') = (u,v) - (<u>,<v>)$) contributes by $\sim$56 % to the total basin-averaged budget (Fig. 1b). As a result of the increased resolution, the time mean of the total KE does not change much over the whole basin (being $\sim$10 % larger than in the twin GLOB4 run), while the eddy contribution is boosted by 40 % by the eddying resolution.

As expected, in the spin-up stage of the integration, the model adjusts from the WOA13 initial conditions towards the new state imposed by the forcing fields and parameter choices. Both basin-mean potential temperature and salinity show a drift with a clear annual cycle (Fig. 1c, d): temperature decreases by $\sim$0.01 °C, while salinity presents a small increase of 0.0013 psu over the 10-year period.

3.1 Mean temperature and salinity

The mean fields of modelled potential temperature and salinity are here validated against the EN3 (the UK Met Office Hadley Centre observational data set; Ingleby and Huddleston, 2007) climatology, both averaged over the same period 2009–2013. As expected, due to the temperature and salinity restoring applied at the ocean surface, the global-mean SST and SSS biases are small (−0.06 for SST and −0.04 for SSS). There are weak cold biases in the tropics, extending over much of the subtropical band, with the largest SST biases (∼ 1 °C warmer) collocated with positive SSS error (0.5–1.5 psu) over the western boundary currents in the Atlantic and North Pacific oceans (not shown). The overall pattern of surface biases is similar between the two models.

The surface biases of models forced by prescribed surface boundary conditions are, to a large degree, constrained by the forcing fields, but the analysis of subsurface fields allows for a stronger test of the model, revealing discrepancies in diapycnal mixing and advection pathways. The time and zonal averages of modelled potential temperature and salinity are shown in Fig. 2a and b, along with their differences from EN3 (Fig. 2c, d). GLOB16 temperature field reproduces the expected large-scale features (Fig. 2a), with cold waters over all depths at high latitudes and warm water at shallow, low latitudes. GLOB16 salinity also follows expectation (Fig. 2b): the low-salinity tongue (34.6 psu) of Antarctic Intermediate Water (AAIW), which sinks to ∼ 1500 m depth between 60–50° S and propagates toward the Equator; a high-salinity (up to 35.2 psu) cell centred around 25° S over the upper 300 m layer; a surface salinity minimum of 34.2 psu at 5–10° N connected to the strong precipitation in the intertropical convergence zone; high-salinity tongue associated with the Mediterranean Sea at about 35° N; low-salinity water over the top 200 m north of 45° N related to the Arctic melt water; and high-salinity (35.2 psu) water below 300 m depth north of 60° N associated with the formation of cold, dense waters in the North Atlantic. All of these features are clearly present in the observation-based climatology (not shown).

The difference field for temperature (Fig. 2c) indicates that the modelled ocean is generally too warm at intermediate depth (100–300 m), with the exception of the AAIW, which is colder by 0.4 °C. The largest differences, propagating down to 1000 m, are located in the Northern Hemisphere from ∼ 40° N (likely due to the Mediterranean Sea) poleward. The locations of the convective site set the positive and negative biases within the band 60–75° N. Compared to EN3 temperature, the upper Arctic Ocean in GLOB16 is too warm (up to ∼ 1.4 °C at ∼ 300 m), mainly due to a warmer Barents Sea inflow. The salinity field reproduced by GLOB16 differs from observations by ∼ 0.15 psu at the most (Fig. 2d). Modelled and observed salinities agree well off Antarctica. The model is saltier by 0.1 psu at about 50° S in the upper 400 m of the water column and by 0.15 psu at the Equator at ∼ 150 m. The model is too saline (up to 0.1 psu) between 200 and 600 m within the 45–55° N latitude band, again likely related to the propagation of the Mediterranean overflow in the Atlantic Ocean. Conversely, it is 0.75 psu fresher in the top layer north of 60° N. The differences between GLOB16 and climatologies for both fields are small below 1500 m depth. Although the overall biases are similar between the two model configurations in many latitude bands, there are some relevant differences (Fig. 2e, f). For instance, the Southern Ocean is generally warmer in GLOB4, with a larger positive salinity bias at ∼ 400 m depth around 50° S. Both models are warm and saline in the above depth range in the northern middle and high latitudes, but the biases differ in magnitude and locations, highlighting the difference in path of the western boundary current. Both models are warmer than observations in the Arctic Ocean: the largest warming is confined in the upper 200 m depth in GLOB16, while the maximum, with a similar rate, is located between 300 and 500 m depth in GLOB4.

3.2 Volume and heat transports

Transports, in particular the meridional overturning circulation (MOC), are frequently used to evaluate the model performance. To provide an overview of the large-scale general circulation of the GLOB16 model, we present the time-mean meridional overturning stream function of the flow for a zonally averaged view. The MOC is shown in Fig. 3, displayed in depth space for the Atlantic and the Indo-Pacific basins, and in density space for the Southern Ocean. In GLOB16, the Atlantic overturning (AMOC, Fig. 3a) reproduces the two overturning cells linked to the formation of North Atlantic Deep Water (NADW) and Antarctic Bottom Water (AABW). The upper cell consists of northward surface flow in the top 1000 m, sinking north of 45° (with ∼ 6 Sv sinking north of the Greenland–Scotland Ridge), and a southward return flow mainly occurring between depths of ∼ 1000 and ∼ 3000 m. It reaches its maximum strength of ∼ 20 Sv at a depth of 1000 m around 35° N. An anticlockwise cell, associated with AABW, fills the deep ocean below 3000 m and reaches ∼ 6 Sv. The cross-equatorial transport is ∼ 16.5 Sv. At lower resolution, the overall transport in the Atlantic Ocean is reduced. The transport weakens in both the upper and lower cells, and the NADW flow extends much deeper as it flows southward, reaching ∼ 3500 m at the Equator (not shown).

Relevant measurements with respect to the mass transport in the Atlantic Ocean and the associated heat transport are provided by the RAPID/MOCHA program (e.g. Cunningham et al., 2007) that makes the net transport across 26.5° N available since spring 2004. Both models are in very good agreement with the RAPID observations at 26.5° N. The GLOB16 overturning strength and variability, computed at that latitude for the simulated decade, is 20.1 ± 2.9 Sv, which is stronger than, but reasonably consistent, with the RAPID

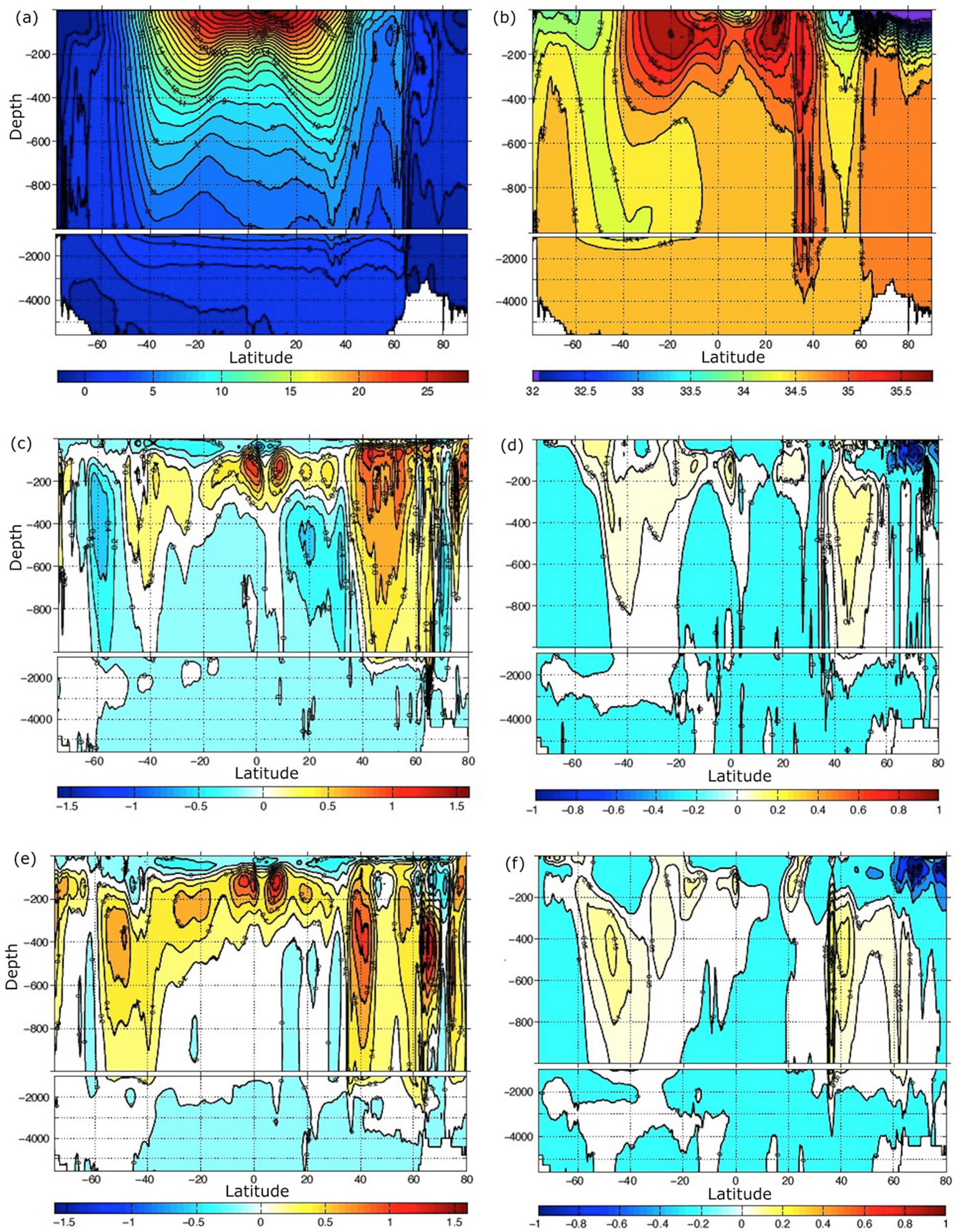

Figure 2. (a, b) GLOB16 zonal mean temperature (left column) and salinity (right column) in years 2009–2013 and **(c, d)** differences with EN3 data set. **(e, f)** As panels **(c, d)** but for GLOB4. Black and Caspian seas are not considered in the zonal mean. The contour interval is 1 °C in panel **(a)**, 0.2 °C in panels **(c, e)**, 0.2 psu in panel **(b)**, and 0.05 psu in panels **(d, f)**.

estimates of 17.0 ± 3.6 Sv observed between April 2004 to December 2013 (McCarthy et al., 2015) (Table 2). The GLOB16 and RAPID mean values for the 2009–2013 period are 19.3 ± 3.1 and 15.6 ± 3.2, respectively (Table 1). In Fig. 3b, we compare the time series of the strength of the AMOC at 26.5° N from the eddying-model integration and the RAPID estimates. At that latitude, GLOB16 simulation realistically reproduces the AMOC temporal variability on seasonal and interannual timescales, although the simulated variability is lower than the observed. The high-resolution model misrepresents the two events of low AMOC observed in 2009 and 2010, when GLOB16 transport exhibits a clear, but much weaker than RAPID, decline. Time series from the twin 1/4° simulation is also shown. The Atlantic overturning transport is generally weaker in GLOB4, with a mean magnitude of 14.9 ± 2.6 Sv over the 10 simulated years, $\sim 25\,\%$ lower than the eddying model. GLOB4 underestimates RAPID values in the first simulated years,

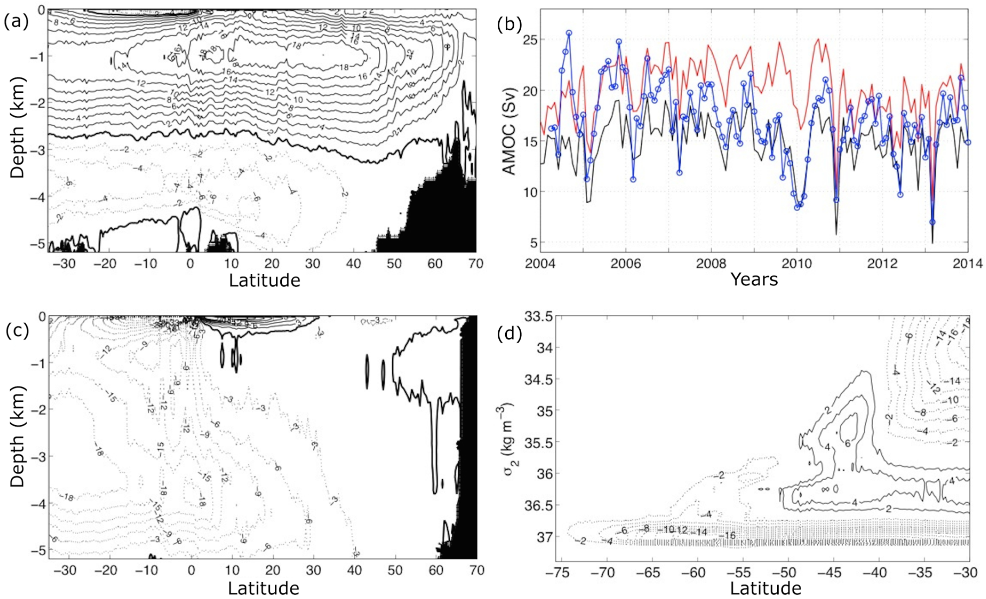

Figure 3. Meridional overturning stream function (in Sv) averaged over the period 2009–2013, calculated in depth space for **(a)** the Atlantic and **(c)** the Indo-Pacific basins and in density space as function of σ_2 for **(d)** the Southern Ocean. The contour interval is 2 Sv in panels **(a, d)** and 3 Sv in panel **(c)**. Thin solid lines represent positive (clockwise) contours; thick solid lines represent zero contours. The stream functions were calculated with 0.5° latitudinal spacing to smooth out small-scale variations. **(b)** Time series of the AMOC at 26.5° N from RAPID observational estimates (blue), GLOB16 (red), and GLOB4 (black) numerical simulations.

Table 1. AMOC and its constituents with standard deviations, averaged within the 2009–2013 period as obtained from RAPID observations and the two models at 26.5° N. The modelled Gulf Stream transports include both the Florida Current and western boundary current contributions.

	RAPID	GLOB16	GLOB4
AMOC	15.6 ± 3.2	19.3 ± 3.1	14.3 ± 2.7
Ekman	3.3 ± 2.3	2.7 ± 2.4	2.7 ± 2.3
Gulf Stream	31.2 ± 2.3	34.9 ± 2.7	32.2 ± 2.1
Upper mid-ocean	-18.9 ± 2.8	-19.8 ± 2.0	-21.3 ± 1.6
Throughflow	0	-1.6 ± 0.5	-0.8 ± 0.5

closely follows RAPID from 2008, and better captures the interannual variability and the 2009–2010 AMOC reductions. Stepanov et al. (2016) suggested that the source of discrepancy between the two models in simulating the AMOC minima at 26.5° N might be related to the RAPID methodology used for the calculation, which does not fully take into account the impact of the recirculation of the subtropical gyre on the mid-ocean transport. Coarser-resolution models, which cannot resolve processes near the western boundary, produce weaker recirculation cell (e.g. Getzlaff et al., 2005; Roussenov et al., 2008; Zhang, 2010). Therefore, in GLOB4, a smaller impact of recirculation and eddies leads to a closer correspondence between the model output and RAPID data. Table 1 shows that the good agreement between GLOB16 and RAPID is true not only for the total AMOC transports but also for its components (the Florida Current, Ekman, and the mid-ocean transports). Details on the decomposition of the AMOC reproduced at 26.5° N are given in Stepanov et al. (2016).

The Indo-Pacific stream function with its intense equatorial upwelling is shown in Fig. 3c. Apart from the uppermost layers, where Ekman transports dominate, the Indo-Pacific is filled by the AABW cell that reaches its maximum values of ∼ 18 Sv between 3000 and 4000 m depth. As expected, the southward flow outcrops in the Northern Hemisphere consistently with intermediate water formation and penetration of water from the circumpolar area near surface and bottom, sandwiching a southward return flow at intermediate depths. Even though the overall structure of the Indo-Pacific MOC does not differ much between the two models, the different resolution corresponds to a ∼ 30 % decrease of the deep overturning (not shown).

The MOC in depth–space is not the most suitable representation of the Southern Ocean overturning circulation. The Deacon cell, for example, is mostly due to a geometrical effect of the east–west slope of the isopycnals and no cross-isopycnal flow is associated with it (Döös and Webb, 1994; Farneti et al., 2015). To account for a better characterization of water mass transports, the Southern Ocean MOC is presented in density space as a function of latitude and potential density $\sigma 2$, referenced to the intermediate depth of 2000 m (Fig. 3d). Three primary cells are identified. The wind-driven subtropical cell is part of the horizontal subtropical gyres and

Table 2. Volume transports (in Sv) through key sections, simulated values averaged in the 2004–2013 period and observed mean values with their standard deviations (when available). Positive values correspond to northward and eastward flows.

	GLOB16	OBSERVED		GLOB4
Max. AMOC at 26.5° N	20.1 ± 2.9	17 ± 3.6	McCarthy et al. (2015)	14.9 ± 2.6
Drake Passage	122.6 ± 5.7	127.7 ± 8.1	Chidichimo et al. (2014)	149.5 ± 9.5
Indonesian throughflow (total at 114° E)	-18.1 ± 2.5	-15 ± 4	Sprintall et al. (2009)	-16.1 ± 2.8
Lombok Strait	-2.2 ± 1.9	-1.8 to -3.2	Sprintall et al. (2009)	–
		-2.6	Gordon et al. (2010)	
Ombai Strait	-4.7 ± 2.2	-2.7 to -5.0	Sprintall et al. (2009)	-5.7 ± 1.4
		-4.9	Gordon et al. (2010)	
Timor Passage	-6.8 ± 1.8	-6.2 to -10.5	Sprintall et al. (2009)	-7.2 ± 1.6
		-7.5	Gordon et al. (2010)	
Mozambique Channel	-23.4 ± 5.4	-29.1	DiMarco et al. (2002)	-20.8 ± 5.8
		-16.7 ± 3.1	Ridderinkhof et al. (2010)	
Bering Strait	1.1 ± 0.5	0.8 ± 0.2	Woodgate et al. (2012)	1.1 ± 0.5
Fram Strait	-2.4 ± 1.0	-2.0 ± 2.7	Schauer et al. (2008)	-1.5 ± 1.2
		-2.3 ± 4.3	Curry et al. (2011)	
Davis Strait	-2.2 ± 0.5	-2.6 ± 1.0	Cuny et al. (2005)	-3.4 ± 0.9
		-1.6 ± 0.5	Curry et al. (2014)	
Denmark Strait overflow	-2.7 ± 0.4	-3.4 ± 1.4	Jochumsen et al. (2012)	-1.4 ± 0.3
FBC overflow	-1.7 ± 0.2	-1.9 ± 0.3	Hansen and Østerhus (2007)	-2.5 ± 0.3

is confined to the lightest density classes. This anticlockwise cell comprises a surface flow spreading poleward to 40° S, compensated by an equatorward return flow. GLOB16 produces a subtropical cell of 18 Sv at 32° S. Below, the upper cell is depicted by the large clockwise circulation, with a time-mean maximum value of 7 Sv. It mainly consists of upper circumpolar deep water that flows at depth southward to $\sim 55°$ S, upwells from 36.5 kg m^{-3} to lighter density classes, and returns northward as AAIW. The anticlockwise lower cell, in the densest layers, reaches 22 Sv and consists of the poleward lower circumpolar deep water and the deeper equatorward AABW. From 60° S to the Antarctic continent, the transport represents the contribution of subpolar gyres in the Weddell and Ross seas. Compared to GLOB16, the Southern Ocean MOC in the eddy-permitting configuration presents a stronger and more extended upper cell but a slightly weaker transport in the subtropical cell and an almost absent deep and dense flow in the lower cell (not shown).

In the North Atlantic, the modelled overturning transport is associated with about 1 PW (1 PW $= 10^{15}$ W) of northward heat flux. The 5-year mean meridional heat transport (MHT) for the Atlantic Ocean simulated by GLOB16 is presented in Fig. 4a; transports from GLOB4 and observational estimates are shown for comparison. It is worth noting that the heat transport magnitude and the location of its maximum are data dependent, although the latitudinal variation is comparable among them. The variation with latitude of the transport realistically follows observed profiles in both configurations with positive magnitude at all latitudes, consistent with heat being carried northward in both hemispheres of the Atlantic Ocean. GLOB16 generally underestimates the heat transport relative to in situ measurements, as also seen in the COREII coarse-resolution models analysed by Danabasoglu et al. (2014) and in the 1/10° climate model by Griffies et al. (2015). However, our eddying-model MHT lies between implied transport estimates: in particular, it is generally below the transport derived from Large and Yeager (2009), but it is always larger than estimates by Trenberth and Fasullo (2008). The MHT maximum is found at $\sim 22°$ N by Large and Yeager (2009) and is more widely distributed between 20 and 30° N in the estimates of Trenberth and Fasullo (2008). In GLOB16, the MHT reaches 1.1 PW at $\sim 24°$, where observations by Lumpkin and Speer (2007) and Ganachaud and Wunsch (2003) are 1.24 ± 0.25 and 1.27 ± 0.15 PW, respectively. GLOB4 MHT lies close to the low estimates by Trenberth and Fasullo (2008), and it is smaller than GLOB16 in most of the basin. The MHT maxima in the two models are collocated in latitude, but the eddy-permitting one presents a ~ 15 % lower peak. In GLOB4, the MHT shows a positive slope between 45 and 55° N, indicating a large gain of heat. It is worth noting that this feature, present in many coarse and eddy-permitting models (e.g. Danabasoglu et al., 2014; Grist et al., 2010), is absent in GLOB16, likely due to a correct path of the simulated North Atlantic Current (Dan-

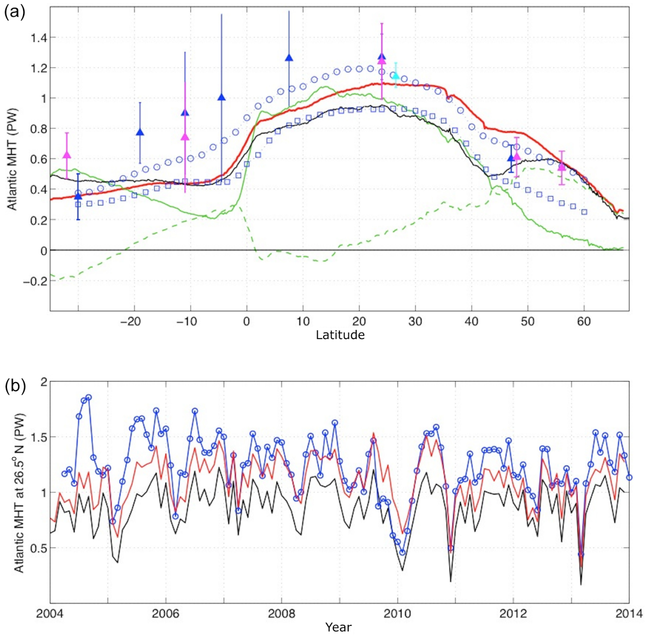

Figure 4. (a) Time-mean Atlantic meridional heat transport (MHT; in PW) as a function of latitude. Red line is the total GLOB16 transport with its overturning (green) and gyre (dashed green) components. Black line represents the total GLOB4 transport. Blue circles (squares) represent implied time-mean transport calculated by Large and Yeager (2009; Trenberth and Fasullo, 2008). Triangles indicate direct estimates with their uncertainty ranges from the 2009–2013 RAPID data (cyan), Ganachaud and Wunsch (2003) (blue), and Lumpkin and Speer (2007) (magenta). **(b)** Times series of the total Atlantic MHT across 26.5° N as estimated by RAPID (blue), GLOB16 (red), and GLOB4 (black).

abasoglu et al., 2014; Treguier et al., 2012), as described in Sect. 3.6. The distinct contributions from the overturning and the gyre circulations to GLOB16 ocean heat transport are also computed (according to Johns et al., 2011) and included in Fig. 4a. The overturning contribution dominates over a large latitude range. This is particularly the case between the Equator and 25° N, where the overturning component is within 1 standard deviation of the mean total heat transport. Poleward, the MOC component drops, while the gyre component increases, explaining the large GLOB16 MHT north of 40° N (in agreement with the eddying climate model results by Griffies et al., 2015). The gyre transport becomes comparable to the overturning contribution at ~45° N and dominating the Atlantic heat transport from 60° N. Apart from the North Atlantic subpolar gyre, the gyre contribution is relevant between 10° S and the Equator, where the gyre and overturning components contribute about equally to the total heat transport. In the eddy-permitting simulation, the overturning and gyre components follow the GLOB16 ones, but the former departs from GLOB16 between 20 and 40° N, being ~0.2 PW weaker, while the latter decreases north of ~35° N to vanish at ~42° N and then increase again, becoming dominant north of 47° N (not shown). This minimum value partially explains the difference between GLOB16 and GLOB4 MHT at 40–45° N.

At 26.5° N, despite a stronger-than-observed AMOC magnitude, GLOB16 underestimates the Atlantic heat transport estimates all through the 10-year RAPID record (2004–2013). Similar behaviour can be seen in many model studies covering a large range of horizontal resolution (e.g. Maltrud and McClean, 2005; Mo and Yu, 2012; Haines et al., 2013; Danabasoglu et al., 2014). The simulated MHT is lower by ~10 % than mean RAPID value that equals 1.24 PW (McCarthy et al., 2015), but the model output agrees, to a greater extent, with the most recent RAPID estimates, which show a decrease of MHT since 2009: the 5-year mean of 1.31 ± 0.27 PW for the pentad 2004–2008 drops by 15 % to 1.14 ± 0.08 PW for the pentad 2009–2013. The variation in time of the modelled and observed MHT at 26.5° N is presented in Fig. 4b. Both runs misrepresent the large summer fluxes in the first 2 years of integration. Afterwards, GLOB16 matches very closely the RAPID magnitude and its variability from 2006 on. The eddy-permitting GLOB4, instead, underestimates both the eddying configuration and the RAPID record with a mean value and variability of 0.87 ± .21 PW.

3.3 Volume transports through critical sections

Although the two models do generally reproduce similar large-scale ocean circulation, performing high-resolution simulations alters strength, shape, and position of the main gyres (Lévy et al., 2010) but especially results in a more accurate representation of narrow boundary currents. To judge the level of agreement between the model velocity fields and the observational data, we list, in Table 2, the time-mean volume transports through well-defined critical straits and passages, evaluated from GLOB16 velocities averaged over the 10 years of integrations, together with GLOB4 values, observation-based estimates, and their sources for each region. It is worth noting that the observational products are based on numbers of assumptions and do not always cover the simulated decade.

The strengths of the GLOB16 transports agree well with observations and are generally within or very close to the limits of observed uncertainty. First, we consider the Drake Passage transport as representative of the large-scale features of the Antarctic Circumpolar Current (ACC). The zonal circumpolar transport drifts from a mean value of 131.2 Sv in 2004 to 117.3 Sv in 2013. The average volume transport is 122.6 (117.2) Sv over the 2004–2013 (2009–2013) period, lower but comparable to the recent observational estimate over the period 2007–2011 by Chidichimo et al. (2014). The time series of the monthly averaged transport, in Fig. 5a, shows a decline of ~10 Sv in the first 3 simulated years, then the drift becomes negligible. As shown by Farneti et al. (2015), at coarser resolution, the mean transport is generally larger than observational estimates. The increase in res-

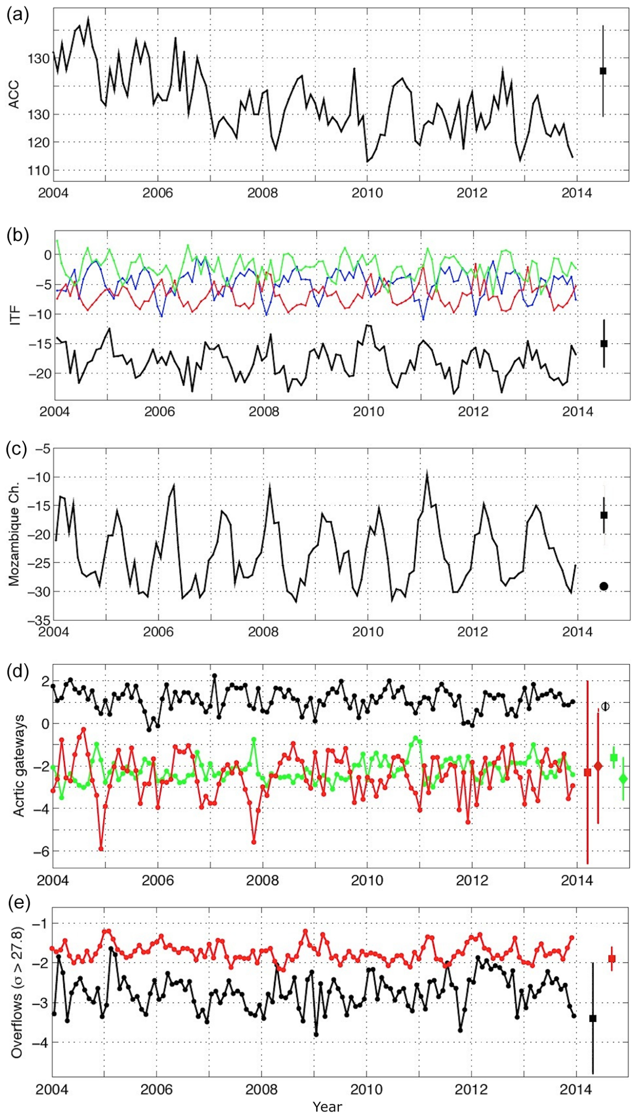

Figure 5. Time series of the monthly averaged volume transport (in Sv) of the **(a)** Antarctic Circumpolar Current (ACC), **(b)** total Indonesian throughflow (ITF) (decomposed in (red) Timor passage, (blue) Ombai strait, (green) Lombok strait), through the **(c)** Mozambique Channel, **(d)** Bering Strait (black), Fram Strait (red), and Davis Strait (green), and **(e)** for dense overflow through Denmark Strait (black) and Faroe Bank Channel (red). Observed values with error bars (as reported in Table 2) are shown.

olution largely improves the mean ACC transport, which is $\sim 20\,\%$ stronger in GLOB4.

The total Indonesian throughflow (ITF) volume transport estimates from the 3-year INSTANT Program corresponds to 15.0 Sv, varying from 10.7 to 18.7 Sv (Sprintall et al., 2009). The mean ITF transport from GLOB16 (computed at 114° E, between Indonesia and Australia) falls within this range but slightly overestimates the observed mean value. The GLOB16 contributions to the Pacific-to-Indian Ocean flow across Lombok, Ombai, and Timor straits follow within the range of minimum and maximum values from INSTANT (Sprintall et al., 2009; Gordon et al., 2010). Beside a weak decrease in the first years of simulation, the ITF has no evident drift over time (Fig. 5b). In GLOB4, the total mean value is closer to observations, but its decomposition is not: the Lombok Strait is closed and is likely compensated by a too strong transport through the Ombai strait.

The southward flux across the Mozambique Channel is 23.4 ± 5.4 (20.8 ± 5.8) Sv in GLOB16 (GLOB4) and, for both models, follows within the broad range of observed estimates, spanning from -29.1 Sv (DiMarco et al., 2002) to -16.7 ± 3.1 Sv (Ridderinkhof et al., 2010). GLOB16 time series, in Fig. 5c, is characterized by a large seasonal cycle and is free from any significant drift.

Comparing the strength of the modelled and observation-based volume transports through the main Arctic Ocean gateways shows that GLOB16 calculations lie within the observed mean values and within the uncertainty range of observations in these areas. The simulated Pacific inflow across the Bering Strait of 1.1 Sv is consistent with observed values in both models, overestimating the recent estimates by Woodgate et al. (2012) to a small degree. The large transport at Bering Strait is common to other NEMO simulations, also at high resolution (e.g. Marzocchi et al., 2015). For the average outflow from the Arctic Ocean (computed across Fram and Davis straits), the simulated 4.6 Sv is indistinguishable from observations, reproducing a correct partitioning of the exports west and east of Greenland. Additionally, 2.4 Sv flows southward across the Fram Strait, compared with an observational estimate of 2 ± 2.7 Sv (Schauer et al., 2008), and 2.2 Sv in the Davis Strait against estimates of 2.6 ± 1 Sv (Cuny et al., 2005) and more recent 1.6 ± 0.5 Sv (Curry et al., 2014). Those transports vary out of phase with each other (Fig. 5d). When the flow is stronger through Fram Strait, it is weaker through Davis Strait and vice versa, indicating that the fluxes out of the Arctic Ocean across those straits partially balance each other. In contrast, GLOB4 reproduces a stronger transport through the Canadian Archipelago and underestimates the Fram Strait component.

The dense and cold overflows from the Nordic Seas supply the densest waters to NADW (e.g. Eldevik et al., 2009) and have a fundamental impact on the circulation in the Irminger and Labrador seas, which are active sites of deep-water formation (e.g. Dickson et al., 2008). To assess whether GLOB16 is capable of reproducing the strength of the overflow (here defined as $\sigma_\theta > 27.8\,\mathrm{kg\,m^{-3}}$), the corresponding volume transport has been calculated both in the Denmark Strait and in the Faroe Bank Channel. The mean transport appears to be consistent with observations in the Denmark Strait, with a mean overflow transport of 2.7 Sv across the Denmark Strait, which slightly underestimates the long-term observed transport of ~ 3 Sv (Macrander et al., 2007; Jochumsen et al., 2012). There is no clear seasonal cycle, and no discernible trend is detected for the whole period (Fig. 5e), as observed by Dickson et al. (2008). The mean transport of dense water across the Faroe Bank Channel is 1.7 Sv with absent trend (Fig. 5e), in accordance with the observed values of ∼ 2 Sv (Hansen and Østerhus, 2007). This consistency builds confidence that the dense water transport processes are realistically simulated in GLOB16. At lower resolution, water masses at the sill depth in the Denmark Strait are too light compared with observations, resulting in a weak overflow in the considered density class, while the Faroe Bank Channel overflow is too dense, with a consequent large transport.

3.4 Mixed layer depth (MLD)

Here we evaluate the winter MLD in both hemispheres. MLDs are computed using a density threshold of 0.03 kg m^{-3} from the near-surface value. The two models represent the mixed layer quite realistically, across the global domain, with similar spatial distribution. Figure 6 shows the MLD reproduced by GLOB16 and GLOB4 for March (September) in the Northern (Southern) Hemisphere calculated for years 2009–2013, alongside the reconstructed climatology of de Boyer Montégut et al. (2004) for the 1994–2002 period. In general, GLOB16 realistically reproduces the expected spatial patterns of the winter surface mixing, with good correspondence between regions of shallow and deep mixed layers. The model reproduces regions of shallow MLDs in the tropics. In the North Atlantic, the sites of winter dense-water formation are realistically located in the subpolar gyre, with the deepest mixing occurring in the Labrador Sea, where it reaches over 2000 m (Fig. 7). In the Nordic Seas, the winter mixing is strong along the path of transformation of Atlantic water in the Norwegian Sea and convective site are reproduced south of Svalbard and in the Iceland Sea with MLDs down to 400 and 1000 m depth, respectively. In the Northern Hemisphere, both runs reproduce mixed layer maxima deeper than observed estimates, as generally seen in NEMO calculations at different resolutions (e.g. Megann et al., 2014; Marzocchi et al., 2015). In GLOB4, the winter mixing in the Nordic Seas is comparable to GLOB16 results, while in the Labrador Sea is shallower than GLOB16 (Fig. 7), but covering a much wider area (Fig. 6). In the austral hemisphere, the deepest winter mixed layer corresponds to the near-zonal bands of deep turbulent mixing along the path of the ACC, where the mixed layer deepens in many instances (Sallée et al., 2010). Maximum values of ∼ 800 m are found in the Pacific basin, not exactly collocated with the observed ones (Fig. 6). Both models have a significant deeper mixed layer in regions of AABW formation, associated with densification of the water masses over the Antarctic continental shelf, a result similarly shown in a recent COREII study assessing 15 ocean/sea-ice models (Downes et al., 2015). The GLOB16 mixed layer reaches depths of 500 and 400 m over the Ross Sea and the Weddell Sea continental shelves, respectively. The time-mean MLD in the Southern Ocean reproduced by GLOB4 is generally shallower than GLOB16 and observations (Fig. 6) but presents deepest maxima close to the Antarctic coast, reaching to over 4000 m in many instances in the first years of integration (Fig. 7).

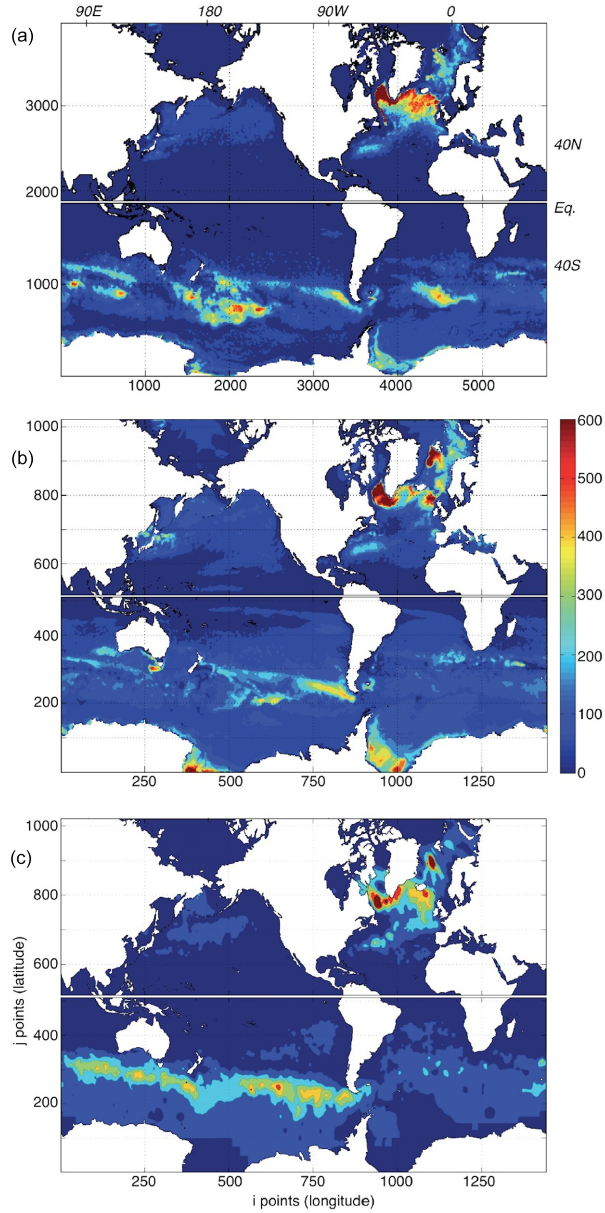

Figure 6. Mixed layer depth (in metres) averaged over March (in the Northern Hemisphere) and September (in the Southern Hemisphere) 2009–2013 from **(a)** GLOB16, **(b)** GLOB4, and **(c)** the de Boyer Montégut et al. (2004) climatology, based on a 0.03 threshold on density profiles. Model outputs are shown on the native grid; observations are interpolated on the eddy-permitting ORCA grid. Numbers of grid points are indicated on the axis, along with indications of latitudes and longitudes.

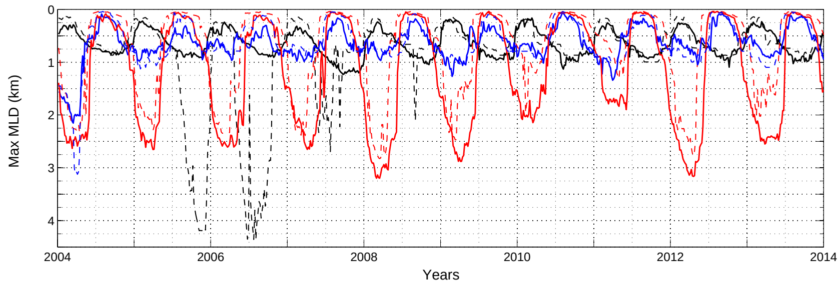

Figure 7. Time series of modelled mixed layer depth (MLD) maxima (in kilometres) in the North Atlantic Ocean (red), the Nordic Seas (blue), and the Southern Ocean (black) from GLOB16 (solid lines) and GLOB4 (dashed).

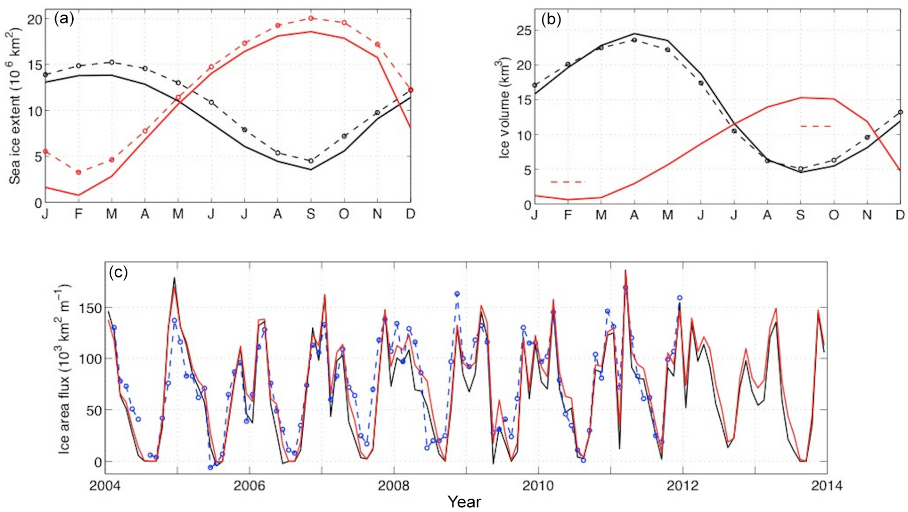

Figure 8. **(a)** Mean GLOB16 seasonal cycles of sea ice extent (10^6 km^2) for the Arctic (black) and Antarctic (red) oceans compared to satellite observations (dashed line) provided by NSIDC. Sea ice extent is defined as the area enclosed in the 10 % sea ice concentration contour. **(b)** Mean seasonal cycles of sea ice volume (10^3 km^3) for the Arctic Ocean (black) compared to PIOMAS reanalysis (dashed line) and for the Antarctica (red) compared to minimum and maximum values from ICESat. **(c)** Sea ice area export (10^3 km^2 month^{-1}) across Fram Strait for GLOB16 (red), GLOB4 (black), and observations (blue).

3.5 Sea ice

Formation and melting of sea ice strongly affect the ocean dynamics both locally in polar regions and in the global ocean, through the contribution of high-latitude processes in deep water production. Here we present sea ice properties and their variability for both hemispheres as simulated by the numerical experiments in comparison with satellite observations. The mean fields are computed over the period 2009–2013, excluding the first 5 years of integration in which the sea ice model is far from the equilibrium. Sea ice extent is defined as the area of the ocean with an ice concentration of at least 10 %.

In Fig. 8a, the mean seasonal cycle of sea ice extent reproduced by GLOB16 is compared with products from passive microwave satellites SSM/I processed at the National Snow and Ice Data Center (NSIDC; Cavalieri et al., 1996) for both the north and south polar regions. In the Arctic Ocean, the simulated mean extent of 9.5×10^6 km^2 and the amplitude of the seasonal cycle of 10.3×10^6 km^2 are, to a great extent, in good agreement with the observations (10.8×10^6 and 10.7×10^6 km^2, respectively). Although the mean sea ice extent is smaller than the satellite estimates by ~ 10 % year-round, the GLOB16 results are largely improved in the end of the run, when the sea ice extent seasonal cycle approaches closely the satellite estimates for both minima and maxima. These results suggest that GLOB16 is able to represent well the sea ice thermodynamics processes after 10 years of integrations.

Figure 8b presents the seasonal cycle of Arctic sea ice volume as simulated in GLOB16 and estimated by the data-assimilative model PIOMAS (Pan-Arctic Ice Ocean Modeling and Assimilation System), which compares well with ICESat and CryoSat2 estimates and can be reasonably considered a proxy for reality (Schweiger et al., 2011). From 2009 on, the GLOB16 sea ice volume (14.4×10^3 km^3) matches very closely PIOMAS values (14.5×10^3 km^3), even

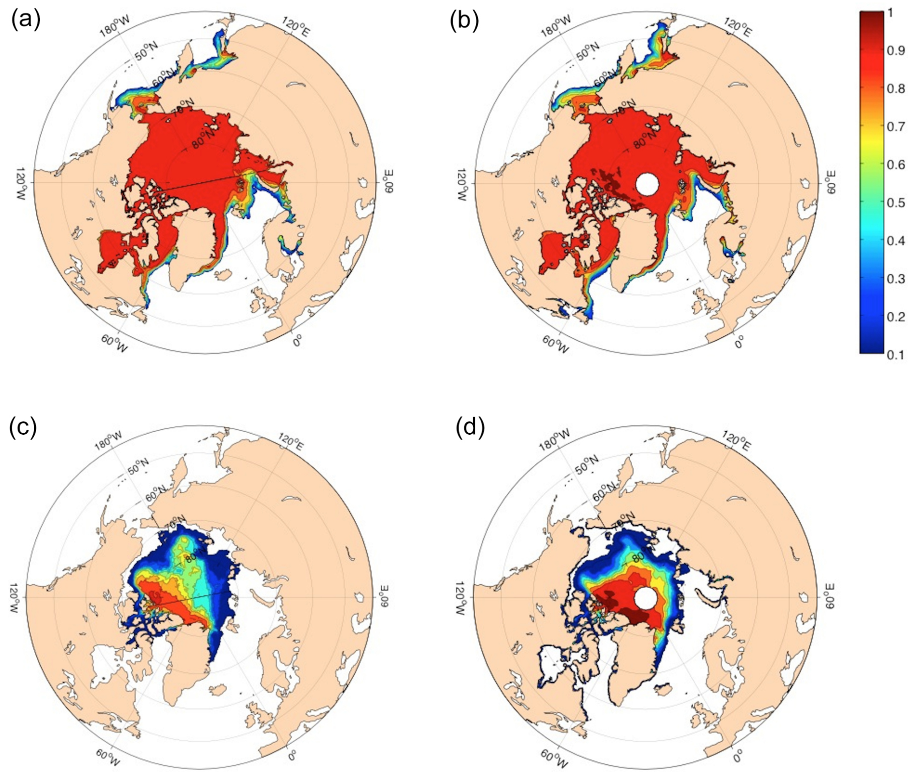

Figure 9. Maximum **(a, b)** and minimum **(c, d)** Arctic sea ice concentration for the period 2009–2013 in GLOB16 (left) and observational data set (right).

if the modelled Arctic sea ice is slightly too thick (thin) during the melting (growing) season. The maximum sea ice volume in GLOB16 is anyway overestimated in winter 2011 and 2012 (not shown), following an increase of thickness due to sea ice drift and then mechanical processes. Overall, the sea ice drift in the Arctic Ocean is similar to what is expected. The transpolar drift and the Beaufort gyre circulation patterns are realistically simulated, but ice velocities are generally too high. Nevertheless, the ice area flux of $74.9 \times 10^3\,\mathrm{km}^2\,\mathrm{month}^{-1}$ across Fram Strait in the simulated decade matches very well to estimates of 75.8 based on using Advanced Synthetic Aperture Radar (ASAR) images and passive microwave measurements (Kloster and Sandven, 2011), probably compensated by lower thickness (Fig. 8c). The Arctic sea ice extent and volume and their variability in time simulated by GLOB4 almost coincide with GLOB16 output, having mean sea ice extent of $9.3(10.9) \times 10^6\,\mathrm{km}^2$ and mean volume of $14.3(7.1) \times 10^3\,\mathrm{km}^3$ in the Northern (Southern) Hemisphere. GLOB4 underestimates the observed ice area export out of the Arctic Ocean through the Fram strait by $\sim 13\,\%$, with a mean value of $66.1 \times 10^3\,\mathrm{km}^2\,\mathrm{month}^{-1}$.

In the Southern Hemisphere, sea ice extent simulated by the two models is again consistent with observations, but GLOB16 (GLOB4) undervalues the total sea ice extent by $1.6(1.8) \times 10^6\,\mathrm{km}^2$. The low maximum in September accelerates the melting process and results in a larger minimum in February (Fig. 8a). At present, no published long-term record of sea ice volume is available for the Southern Hemisphere, making a formal validation of the model skills in simulating sea ice volumes in that region unachievable. We consider recent ICESat laser altimeter observations covering the period 2003–2008 (Kurtz and Markus, 2012) for a qualitative comparison with model outputs, although uncertainties are still high (Kern and Spreen, 2015). Due to the lower minimum sea ice concentration, both models also likely underestimate sea ice thickness and volume in the austral summer, with a possible feedback on the winter sea ice properties. GLOB16 total volume of ice varies substantially over the annual cycle, with a growth of $\sim 14\,000\,\mathrm{km}^3$ in fall larger than the $\sim 8800\,\mathrm{km}^3$ by ICESat (Fig. 8b).

The sea ice edge and the ice geographical distribution are generally well simulated in GLOB16, particularly in winter. Comparison between the simulated fields of sea ice concentration and the satellite-based estimates averaged over 2009–2013 shows that the GLOB16 sea ice distribution in the end of the growing seasons is realistic in both hemispheres (Figs. 9a, b and 10c, d), although the model simulates a more uniform sea ice concentration around Antarctica (Fig. 10c, d). Summer minima are well reproduced in terms of ice edge, but the regional concentration shows differences from the observations (Figs. 9c, d, and 10a, b). In the Arctic Ocean, the GLOB16 reproduces the maximum ice concentration close

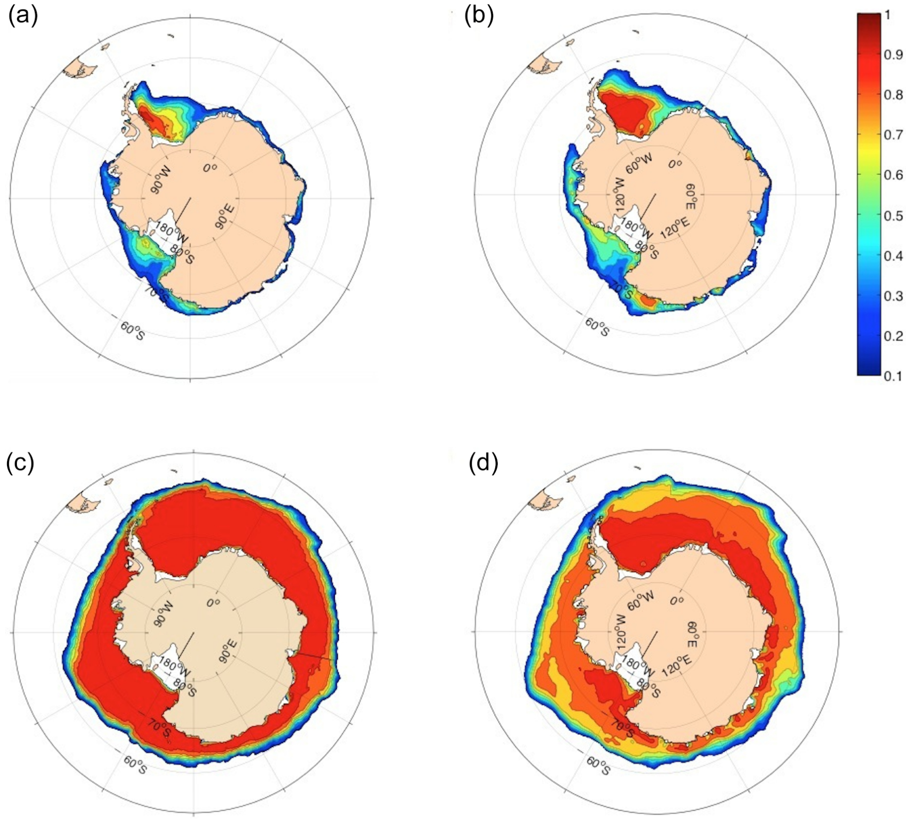

Figure 10. Maximum **(a, b)** and minimum **(c, d)** Antarctic sea ice concentration for the period 2009–2013 in GLOB16 (left) and observational data set (right).

to the Canadian Archipelago, but the spatial structure is misrepresented over a large area, with too low sea ice concentration in the eastern-central sector. This is likely to be caused by the SST restoring and to a generally too warm Atlantic Water inflow.

The spatial distribution of the sea ice in March is correctly reproduced in the Southern Ocean, with the highest value in the Ross Sea and close to the Antarctic Peninsula in the Weddell Sea, where the area of maximum concentration is anyway smaller than the observed one. The too low ice concentration in the austral summer is constantly simulated from the beginning of the run and might be related to a too small sea ice concentration used to initialise the simulation.

3.6 Mesoscale variability

To assess the dynamical capacities of the GLOB16 configuration and to evaluate the gain in representing mesoscale variability due to the higher resolution, Fig. 11 show maps of the sea surface height (SSH) variability, represented by the standard deviation plots, from the eddying ocean compared with the eddy-permitting one and altimetry estimates from AVISO product. The spatial structure and intensity of the SSH variability can be used as indicator of strengths and deficiencies of the mean flow. Both models reproduce the major circulation features estimated from satellite measurements. Large values are collocated with the major current systems associated with the Kuroshio Current, the Gulf Stream, the Loop Current in the Gulf of Mexico, the strong equatorial current system, and, in the southern ocean, the Eastern Australian and the Leeuwin currents, the Brazil and Malvinas current system, the Agulhas Current, and the Antarctic Circumpolar Current. Although GLOB4 does a credible work of reproducing the general observed spatial pattern, it simulates vast areas of low SSH variability in the ocean interior, which indicates weaker flow instabilities and fewer meanders. GLOB16 shows additional instabilities in the upper ocean with a spatial structure richer in mesoscale features that cover most of the ocean surface, and it is more consistent with the observational estimates.

Examination of individual regions can highlight the improvements in GLOB16. In the Northern Hemisphere, the western boundary currents and their extensions are more sharply reproduced at higher resolution. For example, even if the separation point of the Gulf Stream is not largely modified (at $\sim 37°$ N), its path and areal extent differ largely between configurations. The GLOB16 current turns northwestward around the Grand Banks, instead continuing eastward across the Atlantic (as in GLOB4). Further offshore, the

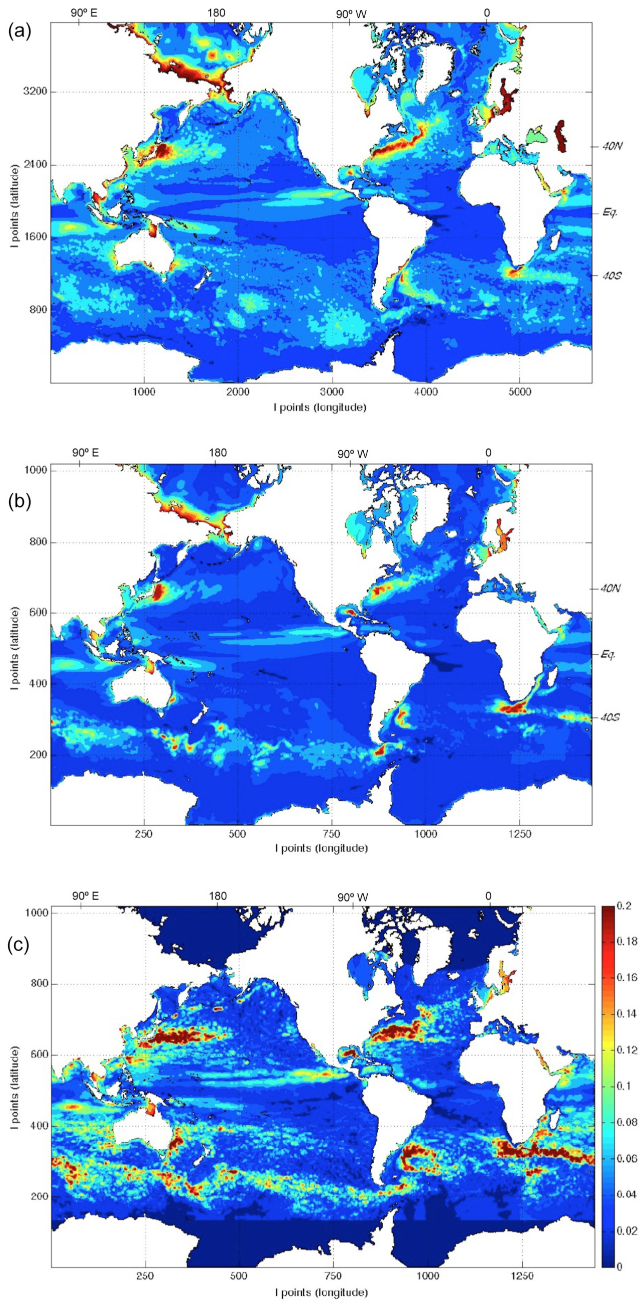

Figure 11. Sea surface height variability (in m) from **(a)** the GLOB16 model, **(b)** the GLOB4 model, and **(c)** AVISO. Modelled fields are shown on the own model grid; observations are interpolated on the eddy-permitting ORCA grid. Numbers of grid points are indicated on the axis, along with indications of latitudes and longitudes.

current separates into a southern branch heading toward the Azores Islands and a second branch flowing towards Newfoundland. This feature is not correctly reproduced in the eddy-permitting case, as in many coarser-resolution models, leading to a cold and fresh bias in the northwestern subpolar gyre. The separation of the Kuroshio Current occurs at about the same latitude ($\sim 36°$ N) in both models, but the high-variability region of the Kuroshio extension extends out to 180° E in GLOB16 in close agreement with data, while it only reaches 160° E in GLOB4.

Some characteristic aspects of the global current systems are still misrepresented, in the eddying run as well. The performance of GLOB16 in reproducing the observed magnitude of the SSH variability is a clear weakness. In many locations in the Southern Ocean, the GLOB16 map shows a wider and more homogeneous distribution of oceanic eddies, but mesoscale turbulence tends to be organized into a large numbers of small and relatively weak patches. The local variability in the 1/16° simulation becomes comparable to or lower than that in the 1/4° simulation and the altimeter map. This is pronounced within the main body of the ACC where local maxima have not substantially and positively increased with resolution. In the Agulhas region, the model shows a band of high variability along the paths of the Mozambique Current, the East Madagascar Current, and the Agulhas retroflection, but the modelled SSH variability is again much less than the observed one. In the Brazil Malvinas convergence region the SSH variability presents a local minimum at about 55° W, 42° S but does only partially resemble the observed C shape. Modelled magnitude departs significantly from observations in the East Australian Current as well.

SSH variance distribution shows strong qualitative similarities to the EKE for the near surface (not shown). In Fig. 12a, we shows the surface EKE, zonally averaged, as calculated from the two simulations and derived from the OSCAR data set (Ocean Surface Current Analyses Real-time; Bonjean and Lagerloef, 2002). OSCAR provides estimates of near-surface ocean currents on a 1/3° grid with a 5-day resolution, combining scatterometer and altimeter data. Quantitatively the models differ significantly from the observations, GLOB16 being the closest. However, both models reproduce higher levels of EKE concentrated at the latitude of the major current system, at the Equator, about 40° N in the Northern Hemisphere, and linked to the ACC and the main western boundary currents in the Southern Ocean. The zonal-averaged EKE profiles emphasize that, despite the local defects, the GLOB16 surface levels of energy exceeds GLOB4 everywhere, except in the equatorial band where the westward extension of the Pacific currents is less pronounced. For the higher-resolution model, the surface EKE increases by $\sim 20\,\%$ relative to GLOB4. Since the two models are forced by identical atmospheric fields, the increase in EKE with resolution arises primarily from increased baroclinic and barotropic instability of the mean flow in the high-resolution model, which tends to generate more meanders and eddies. It has been shown that higher level of near-surface EKE closer to the one derived from OSCAR can be obtained by assimilating in situ and altimeter data in a set of eddy-permitting ORCA025 configurations (Masina et al., 2015). In particular, the assimilation of sea level anomaly has

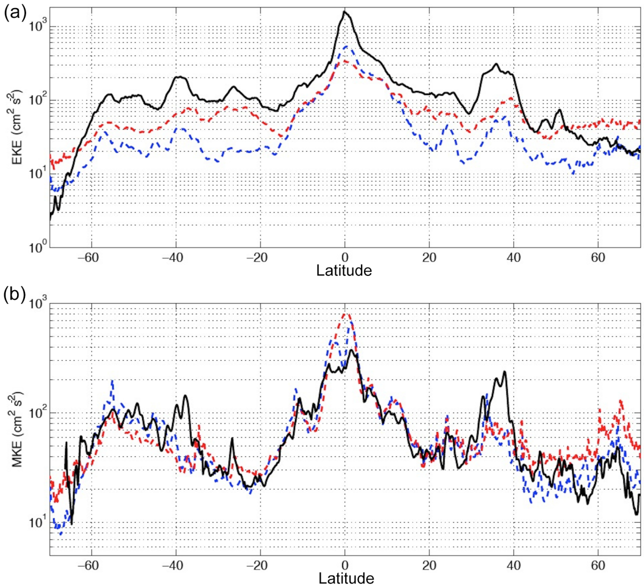

Figure 12. (a) Latitudinal profiles of the global zonal-mean eddy kinetic energy (EKE) (in $cm^2\,s^{-2}$) of the surface flow for 2013 from GLOB16 (red), GLOB4 (blue), and OSCAR (black). Scale is logarithmic. **(b)** As panel **(a)** but for the kinetic energy of the mean flow (MKE) of the surface flow (in $cm^2\,s^{-2}$).

been proven to be effective in introducing mesoscale variability (Storto et al., 2016) underestimated by an eddy-permitting configuration similar to the one used in this work. Our results suggest that the increased resolution of GLOB16 is also able to recover part of the observed variability. However, GLOB16 value represents only ∼ 60 % of the surface EKE estimated from OSCAR. The kinetic energy of the mean flow (MKE) at surface is similar between the models. It increases by 5 % in the 1/16° simulation, reaching 94 % of the observed MKE (Fig. 12b).

4 Conclusions

We have introduced a new global eddying-ocean model configuration, GLOB16, developed at CMCC, and presented an overview from an 11-year simulation. GLOB16 is an implementation of version 3.4 of the NEMO model, with horizontal resolution of at least 1/16° everywhere and 98 vertical levels, together with the LIM2 sea ice model on the same grid.

Overall, the model results are quite satisfactory when compared to observations and the gain due to increased resolution is evident when compared to a coarser-resolution version of the model. Analysis of the model zonally averaged temperature and salinity, MLD, overturning circulation, and associated northward heat transport leads us to conclude that the model average state is realistic and that the model realistically represents the variability in the upper ocean and at intermediate depths. GLOB16 model configuration showed good skill in simulating exchanges of mass between ocean basins and through key passages. The contributions from the individual straits in the exports from the Arctic Ocean are within the uncertainties of the observational estimates. The seasonal cycles of total ice area and volume are close to satellite observations and the sea ice extent distribution is very well reproduced in both hemispheres, although sea ice concentration and thickness can be further improved together with sea ice drift. The model is able to hindcast the position and strength of the surface circulation. Pathways of western boundary currents are better resolved compared to the eddy permitting run. Comparisons between the SSH variability from the model and from gridded satellite observations indicate that the model variability spatial pattern is acceptable, with local maxima and minima in the same locations as observations. However, a clear weakness of this first experiment of GLOB16 model is its ability in reaching the observed magnitude of the SSH variability, especially in the Southern Ocean. This behaviour is most likely related to the coefficients chosen for eddy diffusivity. To improve this aspect, short test experiments are currently being performed employing lower values of the lateral eddy momentum diffusivity. Preliminary results show a more energetic Southern Ocean and an SSH variability much closer to satellite estimates. These results also suggest that more efforts shall be dedicated to sensitivity experiments for detecting the optimal configuration of horizontal and vertical dynamics. It is also possible that the relatively coarse resolution (∼ 0.75°) of the ERA-Interim wind forcing may play a partial role on this underestimation; whether higher-resolution atmospheric products can overcome this feature is to be investigated.

In spite of its shortcomings, we think that GLOB16 represents a significant modelling improvement over the previous configurations of the CMCC global ocean/sea ice models at coarser resolutions. As our first step in exploring the behaviour and fidelity of eddying global models, this simulation sets the necessary groundwork for further, more detailed studies. To potentially ameliorate the model realism, we plan, in the near future, to improve physical parameterizations and include physics upgrades either available or under development in NEMO, such as the full nonlinear free-surface physics, Langmuir turbulence scheme, and vertical mixing parameterizations. We expect that these developments will help address some of the shortcomings identified in this study.

The next phase will be to couple GLOB16 to an ocean/sea ice data assimilation system, similar to that described by Storto et al. (2016). Subsequent to that activity, GLOB16 will constitute the base of a global eddying analysis and short-term forecast system, intended to provide boundary conditions for downscaling and forecasting nested models in the world oceans.

5 Code and data availability

The NEMO model is freely available under the CeCILL public licence. After registration on the NEMO website (http://www.nemo-ocean.eu/), users can access the code (via Subversion, http://subversion.apache.org/) and run the model, following the procedure described in the "NEMO Quick Start Guide". The revision number of the code used for this study is 4510. The CMCC NEMOv3.4 code includes some additional modifications, applied to the base code. In particular, we modified the North Pole folding condition, introducing a more sophisticated optimization of the north fold algorithm (Epicoco et al., 2014), which leads to an extra increase in model performances (up to 20 % time reduction on the used architecture) without altering any physical process. The algorithm is now available in NEMO version 3.6. Interested readers can contact the authors for more information on the CMCC NEMOv3.4 code. The numerical results used here are available under request at CMCC.

Acknowledgements. We thank the two anonymous reviewers for their thorough reading and constructive comments, which helped improving the manuscript. The financial support of the Italian Ministry of Education, University and Research, and Ministry for Environment, Land and Sea through the project GEMINA is gratefully acknowledged. We also acknowledge PRACE for awarding us the project ENSemble-based approach for global OCEAN forecasting (ENS4OCEAN) and providing access to resource on MareNostrum based at the Barcelona Supercomputing Center (Spain). The RAPID data have been loaded from the following web pages: http://www.rapid.ac.uk/rapidmoc and http://www.rsmas.miami.edu/users/mocha. The EN3 subsurface ocean temperature and salinity data were collected, quality controlled, and distributed by the UK Met Office Hadley Centre. The AVISO altimeter products were produced by Ssalto/Duacs and distributed by AVISO, with support from CNES.

Edited by: R. Marsh
Reviewed by: two anonymous referees

References

Barnier, B., Madec, G., Penduff, T., Molines, J. M., Treguier, A. M., Le Sommer, J., Beckmann, A., Biastoch, A., Boning, C., Dengg, J., Derval, C., Durand, E., Gulev, S., Remy, E., Talandier, C., Theetten, S., Maltrud, M., McClean, J., and De Cuevas, B.: Impact of partial steps and momentum advection schemes in a global ocean circulation model at eddy permitting resolution, Ocean Dynam., 56, 543–567, 2006.

Bernie, D., Guilyardi, E., Madec, G., Slingo, J. M., and Woolnough, S. J.: Impact of resolving the diurnal cycle in an ocean–atmosphere GCM. Part 1: a diurnally forced OGCM, Clim. Dynam., 29, 575–590, 2007.

Blanke, B. and Delecluse, P.: Variability of the tropical Atlantic Ocean simulated by a general circulation model with two different mixed layer physics, J. Phys. Oceanogr., 23, 1363–1388, 1993.

Bonjean, F. and Lagerloef, G. S. E.: Diagnostic model and analysis of the surface currents in the tropical Pacific Ocean, J. Phys. Oceanogr., 32, 2938–2954, 2002.

Bouillon, S., Maqueda, M. M., Legat, V., and Fichefet, T.: An elastic-viscous-plastic sea ice model formulated on Arakawa B and C grids, Ocean Model., 27, 174–184, 2009.

Cavalieri, D. J., Parkinson, C. L., Gloersen, P., and Zwally, H.: Sea Ice Concentrations from Nimbus-7 SMMR and DMSP SSM/I-SSMIS Passive Microwave Data. Boulder, Colorado USA: NASA DAAC at the National Snow and Ice Data Center, updated yearly, available at: http://nsidc.org/data/nsidc-0051.html (last access: June 2015), 1996.

Chassignet, E. P., Hurlburt, H. E., Metzger, E. J., Smedstad, O. M., Cummings, J., Halliwell, G. R., Bleck, R., Baraille, R., Wallcraft, A. J., Lozano, C., Tolman, H. L., Srinivasan, A., Hankin, S., Cornillon, P., Weisberg, R., Barth, A., He, R., Werner, F., and Wilkin, J.: U.S. GODAE: Global Ocean Prediction with the HYbrid Coordinate Ocean Model (HYCOM), Oceanography, 22, 64–75, 2009.

Chelton, D., DeSzoeke, R., Schlax, M., El Naggar, K., and Siwertz, N.: Geographical variability of the first baroclinic Rossby radius of deformation, J. Phys. Oceanogr., 28, 433–460, 1998.

Chidichimo, M. P., Donohue, K. A., Watts, D. R., and Tracey, K. L.: Baroclinic transport time series of the Antarctic Circumpolar Current measured in Drake Passage, J. Phys. Oceanogr., 44, 1829–1853, 2014.

Cunningham, S. A., Kanzow, T., Rayner, D., Baringer, M. O., Johns, W. E., Marotzke, J., Longworth, H. R., Grant, E. M., Hirschi, J. J.-M., Beal, L. M., Meinen, C. S., and Bryden, H. L.: Temporal Variability of the Atlantic Meridional Overturning Circulation at 26.5° N, Science, 317, 935–938, 2007.

Cuny, J., Rhines, P., and Kwok, R.: Davis Strait volume, freshwater and heat fluxes, Deep-Sea Res. I, 52, 519–542, doi:10.1016/j.dsr.2004.10.006, 2005.

Curry, B., Lee, C., and Petrie, B.: Volume, freshwater and heat fluxes through Davis Strait, 2004–05, J. Phys. Oceanogr., 41, 429–436, 2011.

Curry, B., Lee, C. M., Petrie, B., Moritz, R. E., and Kwok, R.: Multiyear Volume, Liquid Freshwater, and Sea Ice Transports through Davis Strait, 2004–10, J. Phys. Oceanogr., 44, 1244–1266, 2014.

Dai, A. and Trenberth, K. E.: Estimates of freshwater discharge from continents: latitudinal and seasonal variations, J. Hydrometeorol., 3, 660–687, 2002.

Dai, A., Qian, T., Trenberth, K. E., and Milliman, J. D.: Changes in continental freshwater discharge from 1948–2004, J. Climate, 22, 2773–2791, 2009.

Danabasoglu, G., Yeager, S. G., Bailey, D., Behrens, E., Bentsen, M., Bi, D., Biastoch, A., Böning, C., Bozec, A., Canuto, V. M., Cassou, C., Chassignet, E., Coward, A. C., Danilov, S., Diansky, N., Drange, H., Farneti, R., Fernandez, E., Fogli, P. G., Forget, G., Fujii, Y., Griffies, S. M., Gusev, A., Heimbach, P., Howard, A., Jung, T., Kelley, M., Large, W. G., Leboissetier, A., Lu, J., Madec, G., Marsland, S. J., Masina, S., Navarra, A., Nurser, A. J. G., Pirani, A., Salas y Mélia, D., Samuels, B. L., Scheinert, M., Sidorenko, D., Treguier, A.-M., Tsujino, H., Uotila, P., Valcke, S., Voldoire, A., and Wang, Q.: North Atlantic simulations in

Coordinated Ocean-ice Reference Experiments phase II (CORE-II). Part I: Mean states, Ocean Model., 73, 76–107, 2014.

de Boyer Montégut, C., Madec, G., Fischer, A. S., Lazar, A., and Iudicone, D.: Mixed layer depth over the global ocean: An examination of profile data and a profile-based climatology, J. Geophys. Res., 109, C12003, doi:10.1029/2004JC002378, 2004.

Dee, D. P., Uppala, S. M., Simmons, A. J., Berrisford, P., Poli, P., Kobayashi, S., Andrae, U., Balmaseda, M. A., Balsamo, G., Bauer, P., Bechtold, P., Beljaars, A. C. M., van de Berg, L., Bidlot, J., Bormann, N., Delsol, C., Dragani, R., Fuentes, M., Geer, A. J., Haimberger, L., Healy, S. B., Hersbach, H., Hólm, E. V., Isaksen, L., Kållberg, P., Köhler, M., Matricardi, M., McNally, A. P., Monge-Sanz, B. M., Morcrette, J.-J., Park, B.-K., Peubey, C., de Rosnay, P., Tavolato, C., Thépaut, J.-N., and Vitart, F.: The ERA-Interim reanalysis: configuration and performance of the data assimilation system, Q. J. Roy. Meteor. Soc., 137, 553–597, 2011.

Dickson, R. R., Dye, S., Jónsson, S., Köhl, A., Macrander, A., Marnela, M., Meincke, J., Olsen, S., Rudels, B., Valdimarsson, H., and Voet, G.: The overflow flux west of Iceland: Variability, origins and forcing, in: Arctic-Subarctic Ocean Fluxes: Defining the role of the northern seas in climate, edited by: Dickson, R. R., Meincke, J., and Rhines, P., Springer, Dordrecht, the Netherlands, 443–474, 2008.

DiMarco, S. F., Chapman, P., Nowlin Jr., W. D., Hacker, P., Donohue, K., Luther, M., Johnson, G. C., and Toole, J.: Volume transport and property distributions of the Mozambique Channel, Deep-Sea Res. II , 49, 1481–1511, 2002.

Döös, K. and Webb, D. J.: The Deacon cell and the other meridional cells of the Southern Ocean, J. Phys. Oceanogr., 24, 429–442, 1994.

Downes, S. M., Farneti, R., Uotila, P., Griffies, S. M., Marsland, S. J., Bailey, D., Behrens, E., Bentsen, M., Bi, D., Biastoch, A., Böning, C., Bozec, A., Canuto, V. M., Chassignet, E., Danabasoglu, G., Danilov, S., Diansky, N., Drange, H., Fogli, P. G., Gusev, A., Howard, A., Kelley, M., Ilicak, M., Jung, T., Kelley, M., Large, W. G., Leboissetier, A., Long, M., Lu, J., Masina, S., Mishra, A., Navarra, A., Nurser, A. J. G., Patara, L., Samuels, B. L., Sidorenko, D., Spence, P., Tsujino, H., Wang, Q., and Yeager, S. G.: An assessment of Southern Ocean water masses and sea ice during 1988–2007 in a suite of interannual CORE-II simulations, Ocean Model., 94, 67–94, 2015.

The Drakkar Group: DRAKKAR: developing high resolution ocean components for European Earth system models, in: CLIVAR Exchanges, Special Issue on High Resolution Ocean Climate Modelling, 65, vol. 19, available at: http://www.clivar.org/documents/exchanges-65 (last access: 10 August 2016), July 2014.

Dupont, F., Higginson, S., Bourdallé-Badie, R., Lu, Y., Roy, F., Smith, G. C., Lemieux, J.-F., Garric, G., and Davidson, F.: A high-resolution ocean and sea-ice modelling system for the Arctic and North Atlantic oceans, Geosci. Model Dev., 8, 1577–1594, doi:10.5194/gmd-8-1577-2015, 2015.

Eldevik, T., Nilsen, J. E. Ø., Iovino, D., Olsson, K. A., Sandø, A. B., and Drange, H.: Observed sources and variability of Nordic seas overflow, Nat. Geosci., 2, 406–410, 2009.

Epicoco, I., Mocavero, S., and Aloisio, G.: Performance Optimization of NEMO Oceanic Model at high resolution, Geophysical Research Abstracts, vol. 16, EGU2014-4468, European Geosciences Union General Assemby 2014, 27 April–2 May 2014, Vienna, Austria, 2014.

Farneti, R., Downes, S. M., Griffies, S. M., Marsland, S. J., Behrens, E., Bentsen, M., Bi, D., Biastoch, A., Böning, C., Bozec, A., Canuto, V. M., Chassignet, E., Danabasoglu, G., Danilov, S., Diansky, N., Drange, H., Fogli, P. G., Gusev, A., Hallberg, R. W., Howardh, A., Ilicak, M., Jung, T., Kelley, M., Large, W. G., Leboissetier, A., Long, M., Lu, J., Masina, S., Mishra, A., Navarra, A., Nurser, A. J. G., Patara, L., Samuels, B. L., Sidorenko, D., Tsujino, H., Uotila, P., Wang, Q., and Yeager, S. G.: An assessment of Antarctic Circumpolar Current and Southern Ocean meridional overturning circulation during 1958–2007 in a suite of interannual CORE-II simulations, Ocean Model., 93, 84–120, 2015.

Fichefet, T. and Morales Maqueda, M. A.: Sensitivity of a global sea ice model to the treatment of ice thermodynamics and dynamics, J. Geophys. Res., 102, 12609–12646, 1997.

Fretwell, P., Pritchard, H. D., Vaughan, D. G., Bamber, J. L., Barrand, N. E., Bell, R., Bianchi, C., Bingham, R. G., Blankenship, D. D., Casassa, G., Catania, G., Callens, D., Conway, H., Cook, A. J., Corr, H. F. J., Damaske, D., Damm, V., Ferraccioli, F., Forsberg, R., Fujita, S., Gim, Y., Gogineni, P., Griggs, J. A., Hindmarsh, R. C. A., Holmlund, P., Holt, J. W., Jacobel, R. W., Jenkins, A., Jokat, W., Jordan, T., King, E. C., Kohler, J., Krabill, W., Riger-Kusk, M., Langley, K. A., Leitchenkov, G., Leuschen, C., Luyendyk, B. P., Matsuoka, K., Mouginot, J., Nitsche, F. O., Nogi, Y., Nost, O. A., Popov, S. V., Rignot, E., Rippin, D. M., Rivera, A., Roberts, J., Ross, N., Siegert, M. J., Smith, A. M., Steinhage, D., Studinger, M., Sun, B., Tinto, B. K., Welch, B. C., Wilson, D., Young, D. A., Xiangbin, C., and Zirizzotti, A.: Bedmap2: improved ice bed, surface and thickness datasets for Antarctica, The Cryosphere, 7, 375–393, doi:10.5194/tc-7-375-2013, 2013.

Ganachaud, A. and Wunsch, C.: Large-scale ocean heat and freshwater transport during the World Ocean Circulation Experiment, J. Climate, 16, 696–705, 2003.

Getzlaff, J., Böning, C., Eden, C., and Biastoch, A.: Signal propagation related to the North Atlantic overturning. Geophys. Res. Lett., 32, L09602, doi:10.1029/2004GL021002, 2005.

Good, S. A., Martin, M. J., and Rayner, N. A.: En4: quality controlled ocean temperature and salinity profiles and monthly objective analyses with uncertainty estimates, J. Geophys. Res.-Oceans, 118, 6704–6716, 2013.

Gordon, A. L., Sprintall, J., Van Aken, H. M., Susanto, D., Wijffels, S., Molcard, R., Ffield, A., Pranowo, W., and Wirasantosa, S.: The Indonesian throughflow during 2004–2006 as observed by the INSTANT program, Dynam. Atmos. Oceans, 50, 115–128, 2010.

Griffies, S. M., Winton, M., Anderson, W. G., Benson, R., Delworth, T. L., Dufour, C. O., Dunne, J. P., Goddard, P., Morrison, A. K., Wittenberg, A. T., Yin, J., and Zhang, R.: Impacts on ocean heat from transient mesoscale eddies in a hierarchy of climate models, J. Climate, 28, 952–977, doi:10.1175/JCLI-D-14-00353.1, 2015.

Grist, J. P., Josey, S. A., Marsh, R., Good, S. A., Coward, A. C., de Cuevas, B. A., Alderson, S. G., New, A., Adrian, L., and Madec, G.: The roles of surface heat flux and ocean heat transport convergence in determining Atlantic Ocean temperature variability, Ocean Dynam., 60, 771–790, 2010.

Haines, K., Stepanov, V. N., Valdivieso, M., and Zuo, H.: Atlantic meridional heat transports in two ocean reanalyses evaluated against the RAPID array, Geophys. Res. Lett., 40, 343–348, 2013.

Hallberg, R.: Using a resolution function to regulate parameterizations of oceanic mesoscale eddy effects, Ocean Model., 72, 92–103, 2013.

Hansen, B. and Østerhus, S.: Faroe Bank Channel overflow 1995–2005, Progr. Oceanogr., 75, 817–856, 2007.

Hunke, E. C. and Dukowicz, J. K.: An elastic–viscous–plastic model for sea ice dynamics, J. Phys. Oceanogr., 27, 1849–1867, 1997.

Ingleby, B. and Huddleston, M.: Quality control of ocean temperature and salinity profiles – Historical and real-time data, J. Marine Syst., 65, 158–175, 2007.

IOC, IHO and BODC: Centenary Edition of the GEBCO Digital Atlas, published on CD-ROM on behalf of the Intergovernmental Oceanographic Commission and the International Hydrographic Organization as part of the General Bathymetric Chart of the Oceans, British Oceanographic Data Centre, Liverpool, UK, 2003.

Iovino, D., Storto, A., Masina, S., Cipollone, A., and Stepanov, V.: GLOB16, the CMCC Global Mesoscale-Eddying Ocean, CMCC Research Paper No. 247, doi:10.2139/ssrn.2603170, December 2014.

Jochumsen, K., Quadfasel, D., Valdimarsson, H., and Jónsson, S.: Variability of the Denmark Strait overflow: Moored time series from 1996–2011, J. Geophys. Res., 117, C12003, doi:10.1029/2012JC008244, 2012.

Johns, W. E., Baringer, M. O., Beal, L. M., Cunningham, S. A., Kanzow, T., Bryden, H. L., Hirschi, J. J. M., Marotzke, J., Meinen, C. S., Shaw, B., and Curry, R.: Continuous, Array-Based Estimates of Atlantic Ocean Heat Transport at 26.5° N, J. Climate, 24, 2429–2449, 2011.

Kern, S. and Spreen, G.: Uncertainties in Antarctic sea-ice thickness retrieval from ICESat, Ann. Glaciol., 56, 107–119, 2015.

Kloster K. and Sandven, S.: Ice motion and ice area flux in the Fram Strait at 79° N using ASAR and passive microwave for Feb. 2004–Jul. 2010, Tech. Rep. 322, Nansen Environmental and Remote Sensing Center, Bergen, Norway, 2011.

Kurtz, N. T. and Markus, T.: Satellite observations of Antarctic sea ice thickness and volume, J. Geophys. Res., 117, C08025, doi:10.1029/2012JC008141, 2012.

Large, W. and Yeager, S.: Diurnal to decadal global forcing for ocean sea ice models: the data set and fluxes climatologies, Rep. NCAR/TN-460+STR, National Center for Atmospheric Research, Boulder, Colorado, USA, 2004.

Large, W. and Yeager, S.: The global climatology of an interannually varying air-sea flux data set, Clim. Dynam., 33, 341–364, 2009.

Le Traon, P.-Y., Antoine, D., Bentamy, A., Bonekamp, H., Breivik, L. A., Chapron, B., Corlett, G., Dibarboure, G., DiGiacomo, P., Donlon, C., Faugère, Y., Font, J., GirardArdhuin, F., Gohin, F., Johannessen, J. A., Kamachi, M., Lagerloef, G., Lambin, J., Larnicol, G., Le Borgne, P., Leuliette, E., Lindstrom, E., Martin, M. J., Maturi, E., Miller, L., Mingsen, L., Morrow, R., Reul, N., Rio, M. H., Roquet, H., Santoleri, R., and Wilkin, J.: Use of satellite observations for operational oceanography: recent achievements and future prospects, J. Oper. Oceanogr., 8, Supplement s12–s27, 2015.

Lévy, M., Klein, P., Tréguier, A.-M., Iovino, D., Madec, G., Masson, S., and Takahashi, K.: Modifications of gyre circulation by sub-mesoscale physics, Ocean Model., 34, 1–15, 2010.

Locarnini, R. A., Mishonov, A. V., Antonov, J. I., Boyer, T. P., Garcia, H. E., Baranova, O. K., Zweng, M. M., Paver, C. R., Reagan, J. R., Johnson, D. R., Hamilton, M., and Seidov, D.: World Ocean Atlas 2013, Volume 1: Temperature, edited by: Levitus, S. and Mishonov, A., NOAA Atlas NESDIS 73, Silver Spring, MD, USA, 40 pp., 2013.

Lumpkin, R. and Speer, K.: Global ocean meridional overturning, J. Phys. Oceanogr., 37, 2550–2562, 2007.

Macrander, A., Käse, R. H., Send, U., Valdimarsson, H., and Jónsson, S.: Spatial and temporal structure of the Denmark Strait Overflow revealed by acoustic observations, Ocean Dynam., 57, 75–89, 2007.

Madec, G. and Imbard, M.: A global ocean mesh to overcome the North Pole singularity, Clim. Dynam., 12, 381–388, 1996.

Madec, G. and the NEMO team: Nemo ocean engine – version 3.4, Technical Report ISSN 1288–1619, No. 27, Pôle de modélisation, Institut Pierre-Simon Laplace (IPSL), France, 2012.

Maltrud, M. E. and McClean, J. L.: An eddy resolving global 1/10° ocean simulation, Ocean Model., 8, 31–54, 2005.

Marzocchi, A., Hirschi, J. J.-M., Holliday, N. P., Cunningham, S. A., Blaker, A. T., and Coward, A. C.: The North Atlantic subpolar circulation in an eddy-resolving global ocean model, J. Marine Syst., 142, 126–143, 2015.

Masina, S., Storto, A., Ferry, N., Valdivieso, M., Haines, K., Balmaseda, M., Zuo, H., Drevillon, M., and Parent, L.: An ensemble of eddy-permitting global ocean reanalyses from 1 the MyOcean project, Clim. Dynam., 1–29, doi:10.1007/s00382-015-2728-5, 2015.

McCarthy, G. D., Smeed, D. A., Johns, W. E., Frajka-Williams, E., Moat, B. I., Rayner, D., Baringer, M. O., Meinen, C. S., Collins, J., and Bryden, H. L.: Measuring the Atlantic Meridional Overturning Circulation at 26° N, Prog. Oceanog., 130, 91–111, 2015.

Megann, A., Storkey, D., Aksenov, Y., Alderson, S., Calvert, D., Graham, T., Hyder, P., Siddorn, J., and Sinha, B.: GO5.0: the joint NERC-Met Office NEMO global ocean model for use in coupled and forced applications, Geosci. Model Dev., 7, 1069–1092, doi:10.5194/gmd-7-1069-2014, 2014.

Metzger, E. J., Smedstad, O. M., Thoppil, P. G., Hurlburt, H. E., Cummings, J. A., Wallcraft, A. J., Zamudio, L., Franklin, D. S., Posey, P. G., Phelps, M. W., Hogan, P. J., Bub, F. L., and DeHaan, C. J.: US Navy operational global ocean and Arctic ice prediction systems, Oceanography, 27, 32–43, 2014.

Mo, H.-E. and Yu, Y.-Q.: Simulation of volume and heat transport along 26.5° N in the Atlantic, Atmos. Ocean. Sci. Lett., 5, 373–378, 2012.

Morrow, R. and Le Traon, P. Y.: Recent advances in observing mesoscale ocean dynamics with satellite altimetry, Adv. Space Res., 50, 1062–1076, 2012.

Nurser, A. J. G. and Bacon, S.: The Rossby radius in the Arctic Ocean, Ocean Sci., 10, 967–975, 2014.

Oke, P. R., Griffin, D. A., Schiller, A., Matear, R. J., Fiedler, R., Mansbridge, J., Lenton, A., Cahill, M., Chamberlain, M. A., and Ridgway, K.: Evaluation of a near-global eddy-resolving ocean model, Geosci. Model Dev., 6, 591–615, doi:10.5194/gmd-6-591-2013, 2013.

Reynolds, R. W., Smith, T. M., Liu, C., Chelton, D. B., Casey, K. S., and Schlax, M. G.: Daily high-resolution-blended analyses for sea surface temperature, J. Climate, 20, 5473–5496, 2007.

Ridderinkhof, H., van der Werf, P. M., Ullgren, J. E., van Aken, H. M., van Leeuwen, P. J., and de Ruijter, W. P. M.: Seasonal and interannual variability in the Mozambique Channel from moored current observations, J. Geophys. Res., 115, C06010, doi:10.1029/2009JC005619, 2010.

Roullet, G. and Madec, G.: salt conservation, free surface, and varying levels: a new formulation for ocean general circulation models, J. Geophys. Res., 105, 23927–23942, 2000.

Roussenov, V., Williams, R., Hughes, C., and Bingham, R.: Boundary wave communication of bottom pressure and overturning changes for the North Atlantic, J. Geophys. Res, 113, C08042, doi:10.1029/2007JC004501, 2008.

Sallée, J.-B., Speer, K., Rintoul, S., and Wijffels, S.: Southern Ocean thermocline ventilation, J. Phys. Oceanogr. 40, 509–529, 2010.

Schauer, U., Beszczynska-Möller, A., Walczowski, W., Fahrbach, E., Piechura, J., and Hansen, E.: Variation of flow through the Fram Strait to the Arctic Ocean between 1997 and 2006, in: Arctic–Subarctic Ocean Fluxes, edited by: Dickson, B., Springer, Dordrecht, the Netherlands, 65–85, 2008.

Schweiger, A., Lindsay, R., Zhang, J., Steele, M., and Stern, H.: Uncertainty in modeled arctic sea ice volume, J. Geophys. Res., 116, C00D06, doi:10.1029/2011JC007084, 2011.

Smith, R. D., Maltrud, M. E., Bryan, F., and Hecht, M. W.: Numerical simulation of the North Atlantic Ocean at 1/10, J. Phys. Oceanogr., 30, 1532–1561, 2000.

Sprintall, J., Wijffels, S. E., Molcard, R., and Jaya, I.: Direct estimates of the Indonesian Throughflow entering the Indian Ocean: 2004–2006, J. Geophys. Res., 114, C07001, doi:10.1029/2008JC005257, 2009.

Stepanov, V. N., Iovino, D., Masina, S., Storto, A., and Cipollone, A.: Methods of calculation of the Atlantic meridional heat and volume transports from ocean models at 26.5° N, J. Geophys. Res.-Oceans, 121, 1459–1475, 2016.

Storto, A., Masina, S., and Navarra, A.: Evaluation of the CMCC eddy-permitting global ocean physical reanalysis system (C-GLORS, 1982–2012) and its assimilation components, Q. J. Roy. Meteor. Soc., 142, 738–758, 2016.

Treguier, A. M., Deshayes, J., Lique, C., Dussin, R., and Molines, J. M.: Eddy contributions to the meridional transport of salt in the North Atlantic, J. Geophys. Res., 117, C05010, doi:10.1029/2012JC007927, 2012.

Trenberth, K. E. and Fasullo, J. T.: An observational estimate of inferred ocean energy divergence, J. Climate, 38, 984–999, 2008.

U.S. Department of Commerce: 2-minute Gridded Global Relief Data (ETOPO2v2), National Oceanic and Atmospheric Administration, National Geophysical Data Center, doi:10.7289/V5J1012Q, 2006.

Woodgate, R. A., Weingartner, T. J., and Lindsay, R.: Observed increases in Bering Strait oceanic fluxes from the Pacific to the Arctic from 2001 to 2011 and their impacts on the Arctic Ocean water column, Geophys. Res. Lett., 39, L24603, doi:10.1029/2012GL054092, 2012.

Zalesak, S. T.: Fully multidimensional flux corrected transport for fluids, J. Comput. Phys., 31, 335–362, 1979.

Zhang, R.: Latitudinal dependence of Atlantic meridional overturning circulation (AMOC) variations, Geophys. Res. Lett., 37, L16703, doi:10.1029/2010GL044474, 2010.

Zweng, M. M., Reagan, J. R., Antonov, J. I., Locarnini, R. A., Mishonov, A. V., Boyer, T. P., Garcia, H. E., Baranova, O. K., Johnson, D. R., Seidov, D., and Biddle, M. M.: World Ocean Atlas 2013, Volume 2: Salinity, edited by: Levitus, S. and Mishonov, A., NOAA Atlas NESDIS 74, Silver Spring, MD, USA, 39 pp., 2013.